Supplementary Information

Catalyst to cure: Applications of a new copper-based nanocatalyst in organic synthesis and cancer treatment.

Harini G Sampatkumar,[a] Srushti S Gundakanal,[a] Byresh Gowda,[b] Sudhanva MS,[b] Siddalingeshwar V Doddamani,[c] B S Sasidhar,[c] Alejandro Bugarin, *[d] and Siddappa A Pati*[a]

a. Centre for Nano and Material Sciences, Jain (Deemed-to-be University), Jain Global Campus, Kanakapura, Ramanagaram, Bangalore 562112, India.

b. Adichunchanagiri Institute for Molecular Medicine, Adichunchanagiri Institute of Medical Sciences, Adichunchanagiri University, BG Nagara-571448 Karnataka, India.

c. Chemical Sciences and Technology Division, CSIR-National Institute for Interdisciplinary Science and Technology (NIIST), Thiruvananthapuram 695019, India.

d. Department of Chemistry & Physics, Florida Gulf University, Fort Myers, Florida 33965, United States

Table of contents

1. Materials used, instrumentation and analysis

1.1 Materials

Unless specified otherwise, all reactions were conducted under aerobic conditions using oven-dried glassware with magnetic stirring and heating facilitated by a silicone oil bath. Melamine powder, H_3BO_3, $Cu(NO_3)_2.3H_2O$, nitroarenes, $NaBH_4$, benzonitriles solvents and reagents were procured from Avra, SD Fine and Sigma-Aldrich chemical companies and employed without additional purification. Dill leaves were sourced from local farmers in the Yadavanahalli area of Bangalore, Karnataka, India. Human colon cancer cells, HCT116; were procured from National centre for Cell Sciences (NCCS) Pune, the cell lines were authenticated by STR analysis and the cells were tested for mycoplasma contaminations. Cells were cultured in IMDM, with 2 mM L- glutamine and 1mM Sodium pyruvate (Thermo Fisher Scientific, Inc.; Waltham, MA USA) containing 10% FBS (Gibco; Grand Island, NY, USA). Cells were cultured in a humidified Incubator with 5% CO_2 at 37 °C.

1.2 Instrumentation and analysis

Gas chromatography mass spectroscopy (GC–MS) analysis was performed on Shimadzu (Tokyo, Japan) Make GC–MS-TQ8030 system. Powder X-ray diffraction (*p*-XRD) patterns were obtained using Rigaku X-ray diffraction Ultima-IV. Fourier transform infrared spectra (FT-IR) were recorded with a PerkinElmer Spectrum Two spectrometer. X-ray photoelectron spectroscopy (XPS) was analyzed by using PHI 5000 VersaProbe II, ULVAC-PHI Inc., USA. Thermogravimetric analyzer (TG) (TGA Q500 V20.10 Build 36) was employed for thermogravimetric analysis with a heating rate of 10 °C min^{-1} in N_2 atmosphere. By physisorption of N_2 gas molecules, Brunauer–Emmett–Teller surface areas (BET) were obtained using BELSORP-max, MicrotracBEL, Japan. The total copper content loaded on the nanocatalyst was quantified by inductively coupled plasma optical emission spectroscopy (ICP-OES). Field emission scanning electron microscopy (FE-SEM) along with energy dispersive X-ray spectroscopy (EDS) to observe morphology and determine elemental distributions, respectively, were conducted with a JEOL model JSM7100F. High resolution transmission electron microscopy (HR-TEM) images were obtained using a Jeol/JEM 2100 microscope. Column chromatography was undertaken on silica gel (60–120 mesh) using a proper eluent. Chemical shifts were quoted in parts per million (ppm) referenced to the appropriate solvent peak (DMSO in d6-DMSO: 2.5 ppm). Multiplicities are reported as follows: singlet (s), doublet (d), doublet of doublets (dd), triplet (t), quartet (q), broad (br) and multiplet (m). ^{13}C $\{^1H\}$ NMR was recorded at 500 MHz's. Chemical shifts were reported in ppm referenced to the centre of a multiplet at 40.0 ppm of DMSO. All analytical and spectral data are given for newly synthesized products while for reported compounds; the corresponding references are cited.

2. Experimental section

2.1 Preparation of Dill leaves extract (DLE)

Fresh dill leaves were first washed with tap water and then with distilled water to eliminate any impurities from the surface. The leaves were then cut into small pieces and dried. Once dried, they were blended in an electrical blender. Later, 2.5 g of the ground leaves were then mixed with a 250 mL conical flask containing a mixture of 100 mL EtOH and distilled H_2O (1:1) and stirred for 1 h with a funnel on the mouth of the flask. The ground leaves were then filtered out to obtain a clean extract, which was stored in the refrigerator for future use.

2.2 Synthesis of boron carbon nitride (BCN)

A fine powder was obtained by grinding 1.5 g of melamine and 0.75 g of H_3BO_3. The resulting mixture was then transferred to a crucible and placed inside a muffle furnace. The temperature of the furnace was gradually increased to 550 ℃ at a heating rate of 5 ℃ min^{-1} and held constant for a duration of 4 h. Afterward, the pale yellow BCN product was allowed to cool down to room temperature and rinsed with distilled water to neutral and dried at 70 ℃ before being utilized for further use.

2.3 Synthesis of copper nanoparticles embedded dill leaves extract on boron carbon nitride (CuNPs@DE-BCN)

In the 50 ml of dill leaves extract solution 1 g of BCN was dispersed, sonicated for 30 mins followed by addition of 25 mM of $Cu(NO_3)_2.3H_2O$ and kept for stirring at 80 ℃ for 24 h. The reaction mass was then washed with ethanol. The obtained residue was dried overnight to get olive green coloured nanocatalyst.

2.4 General procedure for the synthesis of tetrazoles using CuNPs@DE-BCN nanocatalyst

A mixture of nitrile (0.5 mmol), and sodium azide (0.63 mmol) were placed in 25-mL round-bottomed flask in PEG-400 (5 mL). The CuNPs@DE-BCN nanocatalyst (2 mol%) was added to the reaction mixture and allowed to react at 120 °C for specified interval time. The progress of the reaction was monitored by TLC. After completion, the reaction mixture was cooled down to RT and the nanocatalyst was removed by filtration and the filtrate was treated with HCl (4N, 10ml) and then extracted with ethyl acetate (2x10 mL). The resultant organic layer was separated, washed with water (2x10 mL) and dried over anhydrous Na_2SO_4. The dried organic layer was concentrated in *vacuo* and purified using *n*-hexane and ethyl acetate as eluents in column chromatography to obtain yields of the respective compounds. Products were characterized by ^{1}H and ^{13}C NMR studies.

2.5 General procedure for the reduction of nitroarenes using CuNPs@DE-BCN nanocatalyst

In a round bottom flask nitrobenzene (0.4 mmol), CuNPs@DE-BCN nanocatalyst (1.3 mol%), $NaBH_4$ (2.8 mmol) was taken. To these, EtOH:H_2O (1:1 v/v, 6 mL) was added and stirred at RT for the

specified time interval. The progress of the reaction was monitored through TLC. After completion of the reaction, the CuNPs@DE-BCN nanocatalyst was separated by centrifugation at 3000 rpm for 6 mins. the obtained supernatant was then extracted with ethyl acetate (2x10 mL), washed with water and the organic phase was dried over anhydrous Na_2SO_4. The dried organic layer was concentrated in *vacuo* and purified using *n*-hexane and ethyl acetate as eluents in column chromatography to obtain yields of the respective compounds. Products were characterized by ^1H NMR.

2.6 Procedure for recovery and recycling of CuNPs@DE-BCN nanocatalyst

On completion of reduction process, the CuNPs@DE-BCN nanocatalyst was recovered from the reaction medium by centrifugation. Then the separated nanocatalyst was washed 2-3 times with ethanol and dried at 40 ℃ for 12 h before using it as such for the next catalytic cycle.

2.7 Apoptotic analysis by Acridine orange / PI Staining:

The Acridine orange / PI double staining assay was performed as described. Briefly, HCT116 cells were seeded in 6-well plates and allowed to attach overnight. Followed by treatment with increasing concentrations of BCN and CuNPs@DE-BCN and incubated for 48 h before subjecting into Acridine orange/PI double staining.

2.8 Hoechst / Propidium iodide analysis:

The Hoechst/PI double staining assay was conducted as described. Briefly, HCT116 cells were seeded in 6-well plates and allowed to attach overnight. Followed by treatment with increasing concentrations of BCN and CuNPs@DE-BCN and incubated for 48 h before subjecting into Hoechst/PI double staining.

2.9 Scratch assay:

HCT116 cells were seeded in 6-well plates and allowed to attach overnight. After reaching 80% confluence a scar was made using micro tip and treated with BCN and CuNPs@DE-BCN and incubated for 24 h and imaged using Olympus microscope.

3. Results & discussion

3.1 Details of characterizations

To identify the components present in the EtOH:H_2O extract of dill leaves, we first conducted a GC-MS analysis. As a result, it revealed key phytochemical components, including phenols, acids, terpenoids and tannins such as 1-tricosanol, phthalic acid 2-methoxyethyl hexadecyl ester, dibutyl phthalate, bis(2-ethylhexyl)phthalate and 2,4-di-tert-butylphenol. These compounds likely contribute to the reduction of Cu(II) to Cu(0) and its stabilization in the nanocatalyst (Fig. S1a). To ascertain the phytochemicals, present in the DLE, a qualitative analysis was performed. This analysis confirmed the

presence of saponins, tannins, phenols, steroids and terpenoids, consistent with existing literature,[1S] as detailed in Table S1 and shown in Fig. S1a.

Table S1. Qualitative analysis of phytochemicals presents in DLE

Analysis	Observation	Result
Test for saponins (a) DLE + distilled H_2O. Shaken well and kept undisturbed for 15 min	Frothing which present on warming	Indicates the presence of saponins.
Test for Tannins CLE + distilled water. Heated on a water bath and filtered. Filtrate + $FeCl_3$	Black solution	Indicates the presence of tannins.
Test for Phenols Aqueous extract + 5% neutral $FeCl_3$	Dark green colour	Indicates the presence of phenols.
Test for Steroids 5 drops of concentrated H_2SO_4 + 1ml extract	Red colour	Indicates the presence of steroids.
Test for terpenoids 1ml extract + 2ml chloroform + 3ml concentrated H_2SO_4	Formation of reddish-brown color at the interface	Indicates the presence of terpenoids.

The crystallographic characteristics of the synthesized BCN and CuNPs@DE-BCN nanocatalyst were evaluated using *p*-XRD (Fig. S1b). BCN displayed two distinct peaks at 2θ = 26.51° and a subtle hump at 43.18°, corresponding to the (002) and (100) planes (JCPDS card No. 52-0233) respectively. In contrast, the CuNPs@DE-BCN nanocatalyst revealed additional peaks at 2θ = 43.37°, 50.41° and 74.05°, indicative of the (111), (200) and (220) planes of Cu(0) NPs (JCPDS card No. 033-1018).

The Fig. S1c exhibits a wide absorption band at approximately 3223 cm^{-1}, which corresponds to N-H stretches. Additionally, there are O-H stretching at 3344 cm^{-1} and B-O deformation at 1184 cm^{-1}, indicating the presence of B-OH groups in BCN nanosheets (NSs).[2S] These groups are likely derived from boric acid precursors. The peaks seen at 1368 cm^{-1} and 1089 cm^{-1} are indicative of the stretching of B-N bonds and the vibrations of cubical B-C structures, providing confirmation of the successful fabrication of BCN NSs. The C=N stretches in BCN NSs are observed at 1646 and 1412 cm^{-1},[3S] similar to bulk graphitic carbon nitride (g-C_3N_4). The two subtle absorption peaks observed in BCN between 809-783 cm^{-1} correspond to the out-of-plane vibrations of the B–N ring, resulting from boron integration into the carbon-nitrogen heterocyclic macrocycle network.[4S, 5S] The FT-IR spectrum of DLE (Fig. S1d) revealed distinct peaks: -OH stretching at 3340 cm^{-1}, asymmetric methyl stretching at 2924 cm^{-1}, C-H stretching of alkanes or secondary amines at 2856 cm^{-1}, primary amine stretching at 1562

cm^{-1} and aromatic amine (C-N stretching) at 1384 cm^{-1}. Additionally, a peak at 1106 cm^{-1} indicated carboxylic acids. These peaks suggest the presence of active compounds like saponins, phenols, terpenoids, steroids and tannins, crucial for reducing Cu(II) to Cu(0) and stabilizing Cu(0) NPs on BCN. Moreover, the nanocatalyst's spectrum confirmed successful synthesis of CuNPs@DE-BCN, while the recycled nanocatalyst's spectra, used in tetrazole synthesis (RT1) and nitroarene reduction (RN1), remained largely unchanged, indicating the retention of its chemical structure.

Based on the data from TGA (Fig. S1e), BCN experiences a steady decrease in mass as the temperature rises. This is caused by the oxidation of carbon[6S] and partial nitrogen oxidation, releasing nitrogen oxides, followed by the formation of boron oxide from unstable boron moieties.[7S] Notably, pure carbon materials, such as carbon fibers, lose total mass at 740°C, but only ~20% under the same conditions after BN doping.[8S] This emphasizes the better aerodynamic stability of BCN in comparison to carbon materials. In addition, the TG curve of the nanocatalyst indicates stability up to 150°C, making it suitable for use in moderate-temperature organic transformations.

The specific surface area of BCN and CuNPs@DE-BCN were measured to be 13.356 $m^2 g^{-1}$ and 22.939 $m^2 g^{-1}$ respectively (Fig. S1f). While the surface area of BCN is relatively low compared to other porous BCN materials,[9S] this is likely due to its bulk synthesis without exfoliation techniques. BCN often forms graphitic or layered structures similar to graphite or *h*-BN, leading to dense stacking and reduced surface accessibility. On the other hand, CuNPs@DE-BCN exhibited type-II isotherm, indicating mesoporous nature with enhanced surface area, likely influenced by the presence of phytochemicals. The BJH pore size distribution plot (Fig. S1g) revealed that CuNPs@DE-BCN has a mean pore diameter of 23.624 nm and a total pore volume of 0.135 $cm^3 g^{-1}$. Further, The exact quantity of Cu present in the synthesized nanocatalyst was quantified by ICP-OES analysis. The Cu loading on the CuNPs@DE-BCN nanocatalyst was found to be 4.19% w/w.

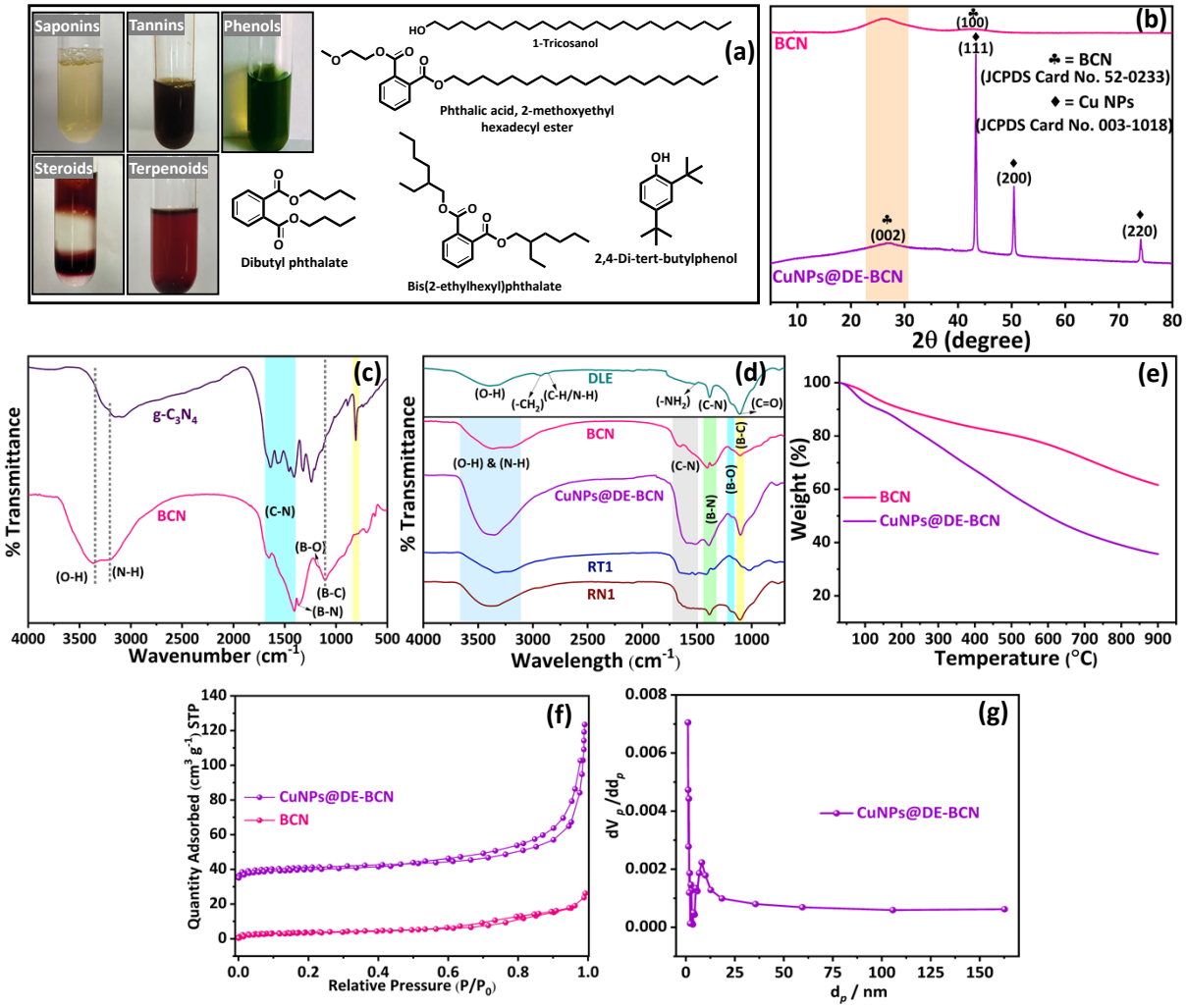

Fig. S1 (a) Images of results of qualitative tests of DLE, (b) *p*-XRD, (c, d) FTIR, (e) TG, (f) Nitrogen adsorption–desorption curves and (g) BJH pore size distribution plot.

The surface micrographs and the porous architecture nature of the prepared materials were eventually obtained by FE-SEM technique and the resultant images were depicted in Fig. S2a and Fig. S2b for BCN and CuNPs@DE-BCN respectively. It was noticed that both BCN and CuNPs@DE-BCN exhibited plain uniform nanosheet structure but when compared with each other Fig. S2b shows the rough surface than that of Fig. S2a. Even after being recycled five and six times for synthesizing 5-phenyl-1*H*-tetrazole and amine respectively, the surface morphology of CuNPs@DE-BCN remained similar to that of the fresh catalyst, as illustrated in Fig. S2c and S2d. However, a noticeable increase in agglomeration was observed after five cycles in the 5-phenyl-1*H*-tetrazole synthesis (Fig. S2c). Furthermore, EDS spectrum (Fig. S2e) showed the presence of boron (B), carbon (C), nitrogen (N), oxygen (O) and Cu elements. The HR-TEM images of CuNPs@DE-BCN nanocatalyst (Fig. S2f & g) clearly showed that Cu NPs uniformly distributed on the BCN sheet as roughly spherical black shapes with an average particles size of 6.52 nm. The polycrystallinity was confirmed from SAED pattern (Fig. S2h). The elemental mapping showed uniform distribution of the elements and Cu NPs (Fig. S2j-o).

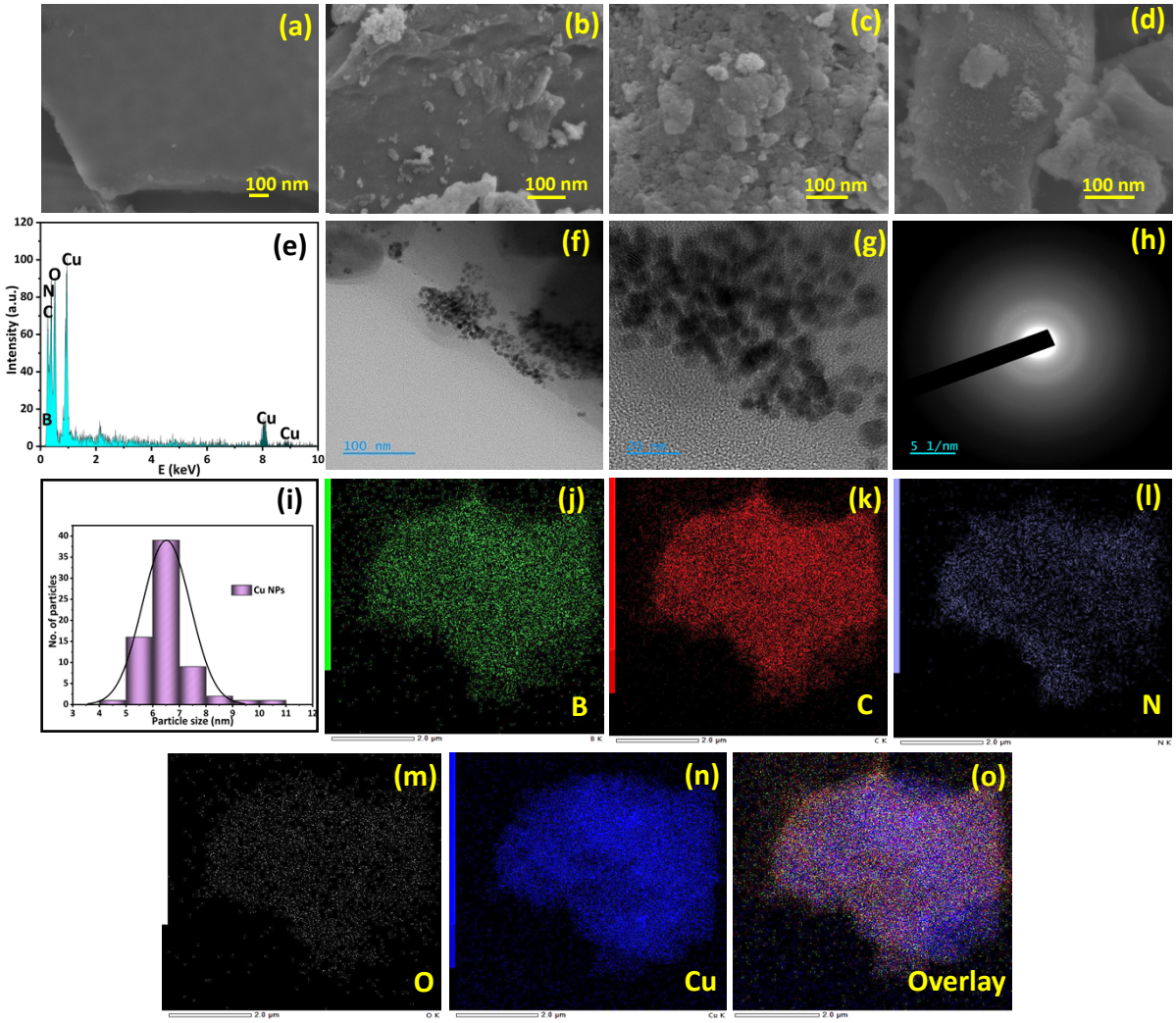

Fig. S2 FE-SEM images of (a) BCN, (b) CuNPs@DE-BCN, (c) four-times recycled CuNPs@DE-BCN used in synthesise of 5-phenyl-1*H*-tetrazole, (d) five-times recycled CuNPs@DE-BCN used amine synthesis, (e) EDS spectrum of CuNPs@DE-BCN, HR-TEM images of (f) BCN, (g) CuNPs@DE-BCN and the corresponding (h) SAED pattern, (i) average particle size distribution and (j–o) elemental mapping.

3.2 Catalytic Activity of CuNPs@DE-BCN for the synthesis of 5-phenyl-1*H*-tetrazole:

Table S2. Optimization reaction condition for the synthesis of 5-phenyl-1*H*-tetrazole

Entry	CuNPs@DE-BCN (mol %)	mmol of Nitrile: NaN_3	Temperature (°C)	Solvent	Time (h)	Yield (%)[a]
1	-	0.5:0.68	120	PEG-400	4	NR
2	2.0	0.5:0.68	120	PEG-400	0.5	98
3	2.0	0.5:0.63	110	PEG-400	2.5	68
4	**2.0**	**0.5:0.63**	**120**	**PEG-400**	**0.5**	**98**
5	2.0	0.5:0.60	120	PEG-400	2.5	72
6	2.3	0.5: 0.63	120	PEG-400	0.5	98

7	1.6	0.5: 0.63	120	PEG-400	1.5	85
8	2.0	0.5: 0.63	Reflux	H_2O	2	Trace
9	2.0	0.5: 0.63	120	DMF	2	73
10	2.0	0.5: 0.63	120	DMSO	2	78
11	2.0	0.5: 0.63	Reflux	CH_3CN	2	Trace
12	2.0	0.5: 0.63	Reflux	Toluene	2	Trace

Bold value indicates the best reaction condition among the sets of reactions performed.
[a]Isolated yield.
NR: no reaction.

When the model reaction was tested under catalyst-free conditions at 120 °C without the nanocatalyst, it failed to proceed, even after an extended reaction time (Table S2, entry 1). On the other hand, the target product was successfully produced in 0.5 h with high yield when the nanocatalyst was present, following the identical reaction conditions (Table S2, entry 2). This finding suggests that the nanocatalyst plays a significant role in the 5-phenyl-1*H*-tetrazole synthesis. Further lowering the reaction temperature to 110 °C resulted in a decreased product yield (Table S2, entry 3). Thus, temperature significantly influences the [3 + 2] cycloaddition reaction of nitriles with NaN_3 ion. Maintaining a 0.63 mmol of NaN_3 resulted in consistent yield (Table S2, entry 4), whereas reducing it to 0.60 mmol led to a noticeable decrease in product yield (Table S2, entry 5). However, increasing the catalyst loading to 2.3 mol% (Table S2, entry 6) did not enhance the product yield, whereas using 1.6 mol% (Table S2, entry 7) of the nanocatalyst resulted in a decrease in the yield. Therefore, 2.0 mol% of the nanocatalyst loading was found to be optimum (Table S2, entry 4). In addition, the effect of solvents on product yield was studied. The reaction duration and product yield were significantly influenced by the solvent selection (Table S2, entries 8–12). At first, we tried to investigate the use of green solvents by conducting the reaction in water; however, it was unsuccessful (Table S2, entry 8). In contrast, DMF and DMSO yielded moderate yields (Table S2, entries 9 and 10), while CH_3CN and toluene exhibited a significantly lower performance (Table S2, entries 11 and 12). Among all tested solvents, PEG-400 emerged as the superior choice, yielding the highest product efficiency and being environmentally benign (Table S2, entry 4). In summary, the optimal conditions for synthesizing 5-phenyl-1*H*-tetrazole were established with a 0.5 mmol of nitrile, 0.63 mmol of NaN_3, 2.0 mol% of nanocatalyst, PEG-400 as the solvent and a reaction temperature of 120 °C.

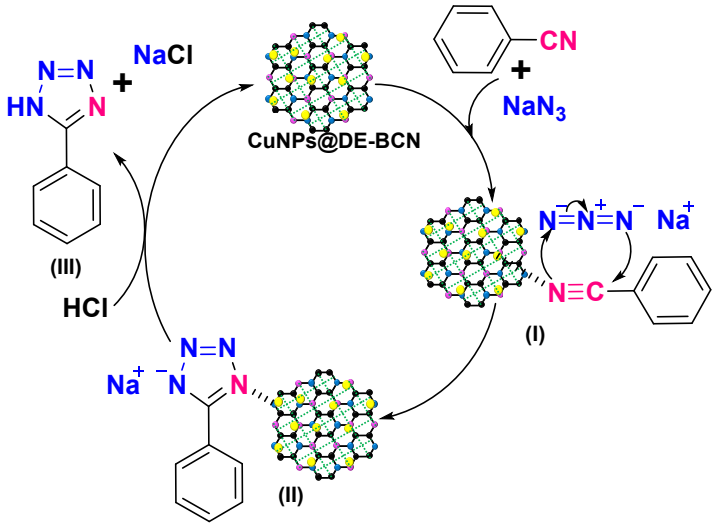

Scheme S1. A plausible reaction mechanism for the 5-phenyl-1*H*-tetrazole.

3.3 Catalytic Activity of CuNPs@DE-BCN for the synthesis of aniline:

Table S3. Optimization of reaction conditions for synthesis of aniline[a]

Entry	CuNPs@DE-BCN (mol%)	$NaBH_4$ (mmol)	Solvent	Times (mins)	Yield (%)[b]
1	1.3	2.8	H_2O	40	70
2	1.3	2.8	EtOH	15	98
3	**1.3**	**2.8**	**EtOH:H_2O (1:1)**	**15**	**98**
4	1.3	2.8	MeOH:H_2O (1:1)	30	82
5	1.3	2.8	Acetonitrile	30	NR
6	1.3	2.8	THF	30	Trace
7	1.3	2.8	Toluene	30	Trace
8	1.3	2.8	EtOH:H_2O (1:3)	15	75
9	1.3	2.8	EtOH:H_2O (1:2)	15	81
10	1.3	2.8	EtOH:H_2O (2:1)	15	98
11	1.3	2.0	EtOH:H_2O (1:1)	30	58
12	1.3	2.4	EtOH:H_2O (1:1)	40	76
13	1.3	-	EtOH:H_2O (1:1)	120	NR
14	-	2.8	EtOH:H_2O (1:1)	30	Trace
15	0.9	2.8	EtOH:H_2O (1:1)	15	56
16	1.2	2.8	EtOH:H_2O (1:1)	15	88

Bold value indicates the best reaction condition among the sets of reactions performed.
[a]Reaction conditions: nitrobenzene (0.4 mmol), room temperature and solvent (6 mL) in air.
[b]Isolated yield.
NR: no reaction.

Optimization of reaction conditions, such as different moles of $NaBH_4$, catalyst loading and solvents were conducted at RT and the results are summarized in Table S3. Initially, the impact of solvent on the catalytic system was examined using various solvents including H_2O, EtOH, EtOH:H_2O(1:1), MeOH:H_2O(1:1), acetonitrile, THF and toluene. The reaction proceeded favourably

with polar protic solvents such as H_2O, EtOH, EtOH:H_2O (1:1)and MeOH:H_2O(1:1) (Table S3, entries 1-4), whereas this trend was not observed with polar aprotic solvents like acetonitrile, THF and toluene (Table S3, entries 5–7). In addition, we have studied the solvent effect of different ratios of (EtOH:H_2O) to make the reaction system more aqueous and environmentally friendly. In cases where the H_2O ratio was increased (Table S3, entries 8 and 9), a decrease in product yield was observed. This could be attributed to solvent interactions, where a higher amount of H_2O alters hydrogen-bonding networks and affects the availability of protons or other active sites, thereby reducing the yield. On the other hand, when the proportion of EtOH was higher (Table S3, entry 10) likely enhances the hydrogen-donating capacity and stabilizes reaction intermediates, resulting in better yields. Furthermore, different moles of $NaBH_4$ were investigated as it acts as both a hydrogen source and reducing agent. The different moles of $NaBH_4$ like 2.0 and 2.4 mmol (Table S3, entries 11 and 12) has influenced the yield of products such as 58 and 76% respectively. Additionally, catalyst loading is crucial in organic reactions, thus the impact of nanocatalyst loading was examined. The optimal quantity of nanocatalyst for nitrobenzene reduction was determined using 0.9, 1.2 and 1.3 mol% of Cu nanocatalyst (Table S3, entries 15 and 16, 3), resulting in product yields of 56, 88 and 98% respectively. In the absence of CuNPs@DE-BCN nanocatalyst as well as $NaBH_4$, the desired product could not be detected, as anticipated (Table S3, entries 13 and 14). Among all conditions, the most favourable results were achieved within 15 mins at RT with 2.8 mmol of $NaBH_4$, using EtOH:H_2O (1:1) (6 mL) as solvent, and employing 1.3 mol% of CuNPs@DE-BCN nanocatalyst (Table S3, entry 3).

Table S4. The reaction of various aromatic arenes with $NaBH_4$[a,b]

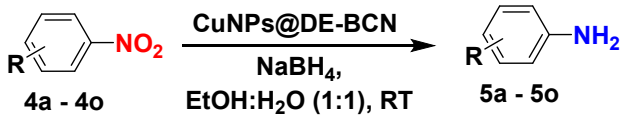

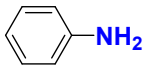 **5a,** 15 min, 98% TON = 30617	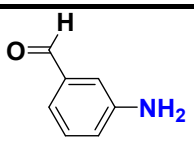 **5b,** 25 min, 88% TON = 22397	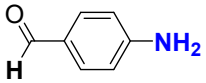 **5c,** 20 min, 92% TON = 23415	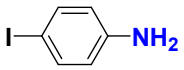 **5d,** 25 min, 90% TON = 13901
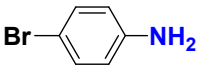 **5e**, 25 min, 52% TON = 9900	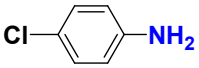 **5f,** 25 min, 38% TON = 9277	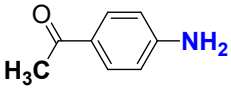 **5g,** 20 min, 95% TON = 22124	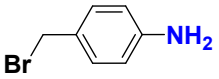 **5h,** 240 min, Trace TON = 2671
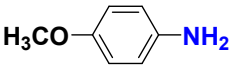 **5i,** 15 min, 92% TON = 23106	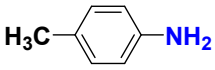 **5j,** 15 min, 96% TON = 23926	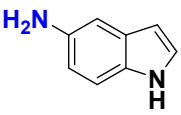 **5k,** 15 min, 92% TON =21822	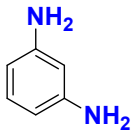 **5l,** 25 min, 90% TON = 20592
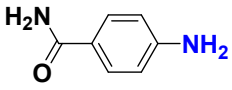 **5m,** 25 min, 95% TON = 21994	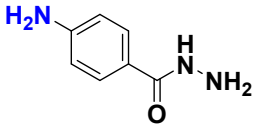 **5n,** 30 min, 98% TON = 20807	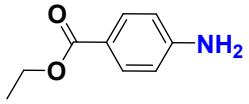 **5o,** 30 min, 96%[C] TON = 18918	

[a]Reaction condition: **4a - 4o** (0.8 mmol), $NaBH_4$ (5.6 mmol), CuNPs@DE-BCN nanocatalyst (2.6 mol%) and EtOH:H_2O (1:1) in air.
[b]Isolated yield after separation by column chromatography; average of two runs.
[c]Drug molecule.

3.4 Recyclability and leaching study of the CuNPs@DE-BCN nanocatalyst

Evaluating recyclability and leaching is crucial for demonstrating the heterogeneity and cost-effectiveness of our prepared nanocatalyst. To this end, we thoroughly examined the recyclability of the CuNPs@DE-BCN nanocatalyst through model reactions for synthesizing 5-phenyl-1*H*-tetrazole (Table S2, entry 4) and aniline (Table S3, entry 3). Remarkably, the nanocatalyst maintained good efficiency, being reused up to five cycles for 5-phenyl-1*H*-tetrazole and six cycles for aniline, achieving consistently good yields as illustrated in Fig. S3a and b. In-depth FT-IR and FE-SEM analyses of the nanocatalyst after these cycles (Fig. S1d and Fig. S2C, d) revealed no significant alterations in chemical composition or morphology, aside from some agglomeration during the 5-phenyl-1*H*-tetrazole synthesis. To assess the leaching behavior, we subjected the nanocatalyst to aniline synthesis under optimized conditions (Table S3, entry 3) for 7 mins, then removed the catalyst and allowed the filtrate to react for an additional 15 mins without the nanocatalyst. TLC monitoring indicated no further

reaction progress, confirming that the nanocatalyst remained intact without leaching into the reaction mixture, thus affirming its heterogeneous nature.

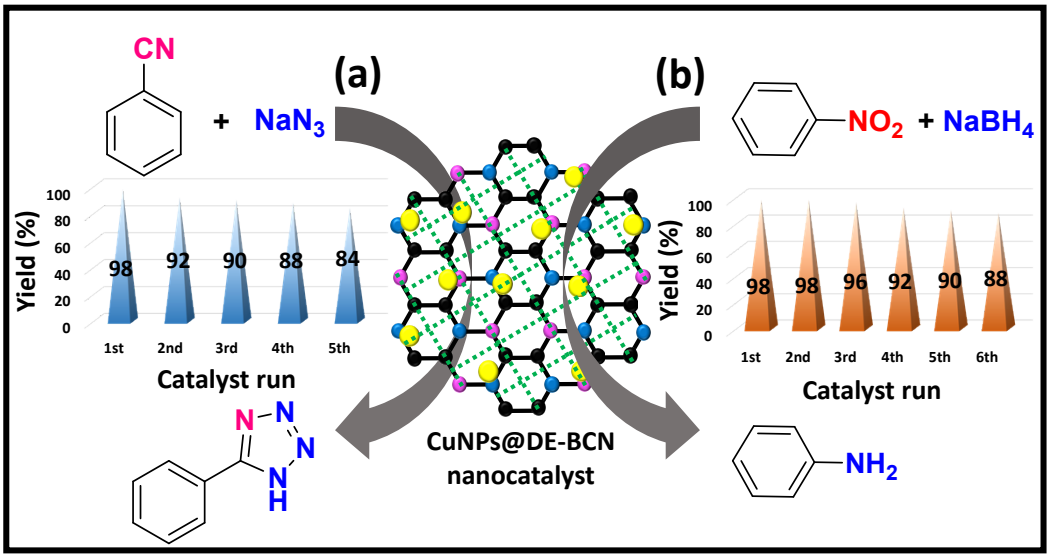

Fig. S3 (a) Five and (b) six times recycled CuNPs@DE-BCN nanocatalyst used for the synthesis of 5-phenyl-1*H*-tetrazole and aniline respectively.

3.5 Comparison of catalysts in synthesis of 5-phenyl-1*H*-tetrazole and aromatic amines

In demonstrating the impressive capabilities of the CuNPs@DE-BCN nanocatalyst, we compared its performance in synthesizing 5-phenyl-1*H*-tetrazole and aromatic amines with other reported literature (Table S5 and S6 respectively). Our findings reveal that the CuNPs@DE-BCN nanocatalyst demonstrates superior catalytic activity in a green medium. This nanocatalyst offers numerous advantages, including shorter reaction times, moderate reaction condition, the use of green solvents such as PEG-400 and EtOH:H_2O (1:1) , excellent selectivity, reusability, cost-effectiveness.

Table S5. Comparison of results for CuNPs@DE-BCN nanocatalyst with other catalysts for the synthesis of 5-phenyl-1*H*-tetrazole.

Entry	Catalyst	Solvent	Temp (°C)	Time (h)	Yield (%)	References
1	Pd-SMTU@boehmite	PEG-400	120	2.5	95	10S
2	$AgNO_3$	DMF	120	5	83	11S
3	Fe_3O_4/ZnS HNSs	DMF	120	24	81.1	12S
4	Fe_3O_4@SiO_2/Salen Cu(II)	DMF	120	7	90	13S
5	CoY Zeolite	DMF	120	14	90	14S
6	Cu–Zn alloy nanopowder	DMF	120	10	95	15S
7	Cu(II)-Adenine-MCM-41	PEG-400	130	5	92	16S
8	**CuNPs@DE-BCN nanocatalyst**	**PEG-400**	**120**	**0.5**	**98**	**Present work**

Bold value indicates the best reaction condition among the previously published catalysts.

Table S6. Comparison of results for CuNPs@DE-BCN nanocatalyst with other catalysts for the synthesis of aromatic amines.

Entry	Catalyst	Solvent	Temp (°C)	Time (mins)	Yield (%)	References
1	Au / $Fe(OH)_x$	Water	100	180	99	17S
2	PdNPs@g-C_3N_4-BLE	MeOH:H_2O (1:1)	RT	2	98	18S
3	$RuCl_2$ PPh_3	Dioxane	60	960	96	19S
4	$CuFe_2O_4$-G (25%)	EtOH:H_2O (1:1)	70	30	92	20S
5	$Cu_{6/7}Co_{1/7}Fe_2O_4$-G (0.25)	EtOH:H_2O (1:1)	70	25	95	21S
6	Cu / Fe_3O_4 NPs	EtOH:H_2O (1:1)	50	180	95	22S
7	CuO NPs	H_2O	70	10	95	23S
8	**CuNPs@DE-BCN**	**EtOH:H_2O (1:1)**	**RT**	**15**	**98**	**Present work**

Bold value indicates the best reaction condition among the previously published catalysts.

3.6 BCN and CuNPs@DE-BCN mitigates migration of colorectal cancer cells:

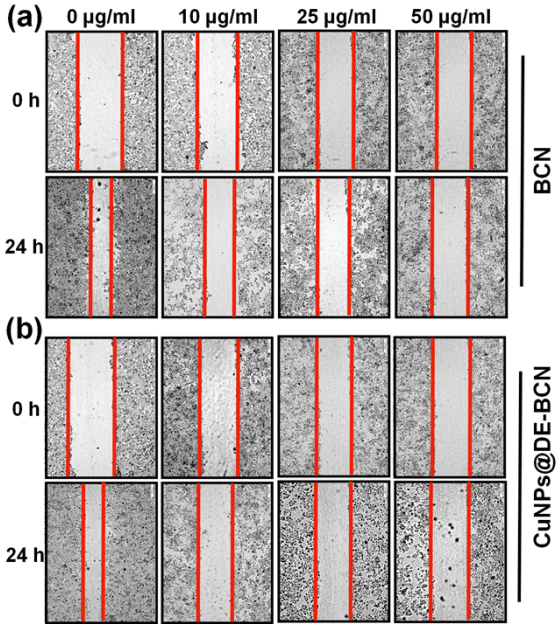

Fig. S4 (a, b) Effects of BCN and CuNPs@DE-BCN on migration: cells treated with materials were incubated for 24 h and imaged using Olympus microscope bright field images of recovered scars. Scale bar was 200 µm.

4. Spectroscopic data of newly obtained Products

5-phenyl-1*H*-tetrazole (3a):

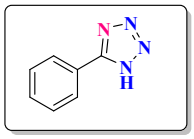

^{1}H NMR (500 MHz, DMSO-d6, ppm): δ 8.00 (br, 2H), 7.47 (br, 3H); ^{13}C NMR δ 131.09, 129.32, 127.07, 126.92.

5-(4-acetyl)-1*H*-tetrazole (3b):

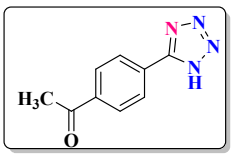

^{1}H NMR (500 MHz, DMSO-d6, ppm): δ 8.12 (dd, J = 11 Hz, 4H), 2.60 (s, 3H); ^{13}C NMR δ 197.93, 138.91, 129.69, 128.79, 127.70, 27.26, 14.48.

5-(4-formylphenyl)-1*H*-tetrazole (3c):

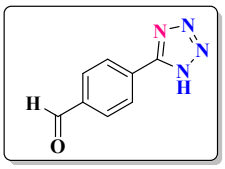

^{1}H NMR (500 MHz, DMSO-d6, ppm): δ 9.84 (s, 1H), 8.00 (d, J = 8 Hz, 2H), 7.86 (d, J = 2.5 Hz, 2H); ^{13}C NMR δ 193.05, 155.90, 138.03, 130.79, 130.00, 128.03.

5-(4-bromophenyl)-1*H*-tetrazole (3d):

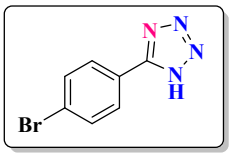

^{1}H NMR (500 MHz, DMSO-d6, ppm): δ 7.97 (d, J = 7.5 Hz), 7.80 (d, J = 7.0 Hz, 2H); ^{13}C NMR δ 155.48, 132.91, 129.31, 125.06, 124.05.

5-(2-chlorophenyl)-1*H*-tetrazole (3e):

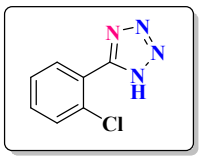

^{1}H NMR (500 MHz, DMSO-d6, ppm): δ 7.82 (d, J = 7.5 Hz, 1H), 7.74 (d, J = 8 Hz, 1H), 7.64 (t, J = 7.5 Hz, 1H), 7.57 (t, J = 7.5 Hz, 1H); ^{13}C NMR δ 133.10, 132.45, 132.23, 130.90, 128.26, 124.62.

5-(4-fluorophenyl)-1*H*-tetrazole (3g):

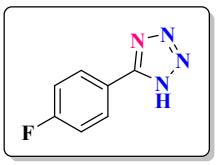

^{1}H NMR (500 MHz, DMSO-d6, ppm): δ 8.08 (t, J = 6.5 Hz, 2H), 7.44 (t, J = 8.5 Hz, 2H); ^{13}C NMR δ 165.10, 163.12, 155.17, 129.94, 121.94, 117.10, 116.92.

5-(3-nitrophenyl)-1*H*-tetrazole (3h):

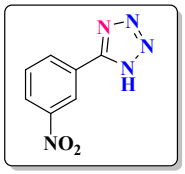

^{1}H NMR (500 MHz, DMSO-d6, ppm): δ 8.83 (s, 1H), 8.47 (d, J = 7.5 Hz, 1H), 8.42 (d, J = 8.0 Hz, 1H), 7.91 (t, J = 8 Hz, 1H); ^{13}C NMR δ 155.43, 148.74, 133.54, 131.71, 126.99, 126.07, 121.98.

5-(4-methoxyphenyl)-1*H*-tetrazole (3i):

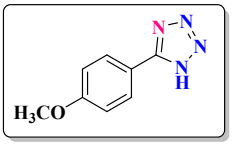

^{1}H NMR (500 MHz, DMSO-d6, ppm): δ 7.96 (d, J = 7.5 Hz, 2H), 7.16 (d, J = 7.5 Hz, 2H), 3.84 (s, 3H); ^{13}C NMR δ 160.52, 155.20, 129.09, 116.76, 115.31, 55.91.

5-(4-hydroxyhenyl)-1*H*-tetrazole (3j):

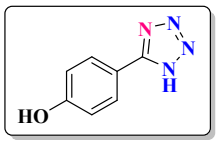

^{1}H NMR (500 MHz, DMSO-d6, ppm): δ 10.18 (br s, 1H), 7.87 (d, J = 8 Hz, 2H), 6.96 (d, J = 8 Hz, 2H); ^{13}C NMR δ 160.57, 155.02, 129.20, 116.60, 115.70.

2-chloro-3-(1*H*-tetrazol-5-yl) pyridine (3l):

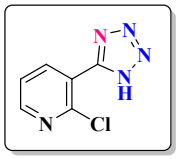

^{1}H NMR (500 MHz, DMSO-d6, ppm): δ 8.64 (br, 1H), 8.31 (d, J = 7.5 Hz, 1H), 7.67 (br, 1H); ^{13}C NMR δ 197.93, 175.05, 138.91, 129.69, 128.79, 127.70.

5-(thiophen-2-yl)-1*H*-tetrazole (3m):

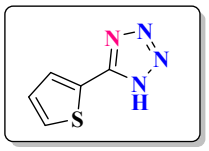

^{1}H NMR (500 MHz, DMSO-d6, ppm): δ 7.88 (br, 1H), 7.80 (br, 1H), 7.29 (br, 1H); ^{13}C NMR δ 151.81, 130.81, 129.61, 129.07, 125.94.

4-aminobenzamide (5m):

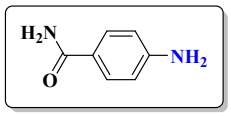

^{1}H NMR (500 MHz, DMSO-d6, ppm): δ 7.58 (d, J = 7.5 Hz, 2H), 6.85 (br s, 2H), 6.52 (d, J = 8.0 Hz, 2H), 5.60 (s, 2H).

4-aminobenzohydrazide (5n):

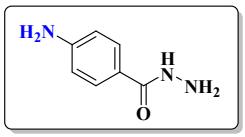

^{1}H NMR (500 MHz, DMSO-d6, ppm): δ 9.27 (s, 1H), 7.53 (d, J = 8.0 Hz, 2H), 6.52 (d, J = 8.0 Hz, 2H), 5.57 (s, 2H), 4.52 (br, 2H).

Ethyl-4-aminobenzoate [Benzocaine] (5o):

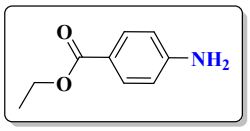

^{1}H NMR (500 MHz, DMSO-d6, ppm): δ 7.67 (d, J = 3.5 Hz, 2H), 6.59 (d, J = 8.0 Hz, 2H), 5.94 (s, 2H), 4.20 (dd, J = 6.5 Hz, 2H), 1.26 (t, J = 7.0 Hz, 3H).

Phenylamine [Table S4, 5a], 3-Aminobenzaldehyde [Table S4, 5b], 4-Aminobenzaldehyde [Table S4, 5c], 4-Iodoaniline [Table S4, 5d], 1-(4-Aminophenyl) ethenone [Table S4, 5g], 4-Aminoanisole [Table S4, 5i], 4-Amino-1-methylbenzene [Table S4, 5j], 5-Aminoindole [Table S4, 5k], Benzene-1,3-diamine [Table S4, 5l], all these products are confirmed by comparing with our previously reported research.[18S]

5. References

1S O. A. Ushie, A. I. Onen, O. C. Ugbogu, P. A. Neji and V. B. Olumide, *ChemSearch J.*, 2016, **7(2)**, 64-69.

2S J. Wu, L. Wang, B. Lv and J. Chen, *ACS Appl. Mater. Interfaces.*, 2017, **9(16)**, 14319-14327.

3S F. Guo, P. Yang, Z. Pan, X. N. Cao, Z. Xie and X. Wang, *Angew. Chem.*, 2017, **129(28)**, 8343-8347.

4S T. Zhang, S. Zeng, G. Wen and J. Yang, *Microporous Mesoporous Mater.*, 2015, **211**, 142-146.

5S K. Sivaprakash, M. Induja and P. G. Priya, *Mater. Res. Bull.*, 2018, **100**, 313-321.

6S M. Jalaly, F. José Gotor, M. Semnan and M. Jesús Sayagués, *Sci. Rep.*, 2017, **7(1)**, 3453.

7S S. Bernard and P. Miele, *Materials*, 2014, **7(11)**, 7436-7459.

8S Z. Xu, Y. Chen, W. Li, J. Li, H. Yu, L. Liu, G. Wu, T. Yang and L. Luo, *RSC Adv.*, 2018, **8(32)**, 17944-17949.

9S D. Portehault, C. Giordano, C. Gervais, I. Senkovska, S. Kaskel, C. Sanchez and M. Antonietti, *Adv. Funct. Mater.*, 2010, **20(11)**, 1827-1833.

10S P. Moradi and A. Ghorbani-Choghamarani, *Appl. Organomet. Chem.*, 2017, **31(5)**, e3602.

11S P. Mani, A. K. Singh and S. K. Awasthi, *Tetrahedron Lett.*, 2014, **55(11)**, 1879-1882.

12S G. Qi, W. Liu and Z. Bei, *Chin. J. Chem.*, 2011, **29(1)**, 131-134.

13S F. Dehghani, A. R. Sardarian, M. Esmaeilpour, *J. Organomet. Chem.*, 2013, **743**, 87-96.

14S V. Rama, K. Kanagaraj and K. Pitchumani, *J. Org. Chem.*, 2011, **76(21)**, 9090-9095.

15S G. Aridoss, and K. K. Laali*, Eur. J. Org. Chem.*, 2011, 6343-6355.

16S M. Nikoorazm, A. Ghorbani-Choghamaranai, M. Khanmoradi and P. Moradi, *J. Porous Mater.*, 2018, **25**, 1831-1842.

17S L. Liu, B. Qiao, Z. Chen, J. Zhan and Y. Deng, *ChemComm*., 2009, **6**, 653-655.

18S H. G. Sampatkumar, N. Rhakho, V. Kandathil, M. Kempasiddaiah, A. M. Shirahatti, R. B. Dateer, A. K. Samal and S. A. Patil, *Catal. Letters.*, 2024, **154(2)**, 352-365.

19S T. Schabel, C. Belger and B. Plietker, *Org. Lett.*, 2013, **15(11)**, 2858-2861.

20S H. Zhang, S. Gao, N. Shang, C. Wang and Z. Wang, *RSC Adv.*, 2014, **4(59)**, 31328-31332.

21S H. Zhang, Y. Zhao, W. Liu, S. Gao, N. Shang, C. Wang and Z. Wang, *Catal. Commun.*, 2015, **59**, 161-165.

22S S. M. Sajadi, M. Nasrollahzadeh and M. Maham, *J. Colloid Interface Sci.*, 2016, **469**, 93-98.

23S A. Lucchesi Schio, M. R. Farias Soares, G. Machado and T. Barcellos, *ACS Sustain. Chem. Eng.*, 2021, **9(29)**, 9661-9670.

***Appendix I*: Spectral copies of ^{1}H and ^{13}C NMR of compounds obtained in this study**

5-phenyl-1*H*-tetrazole (3a):

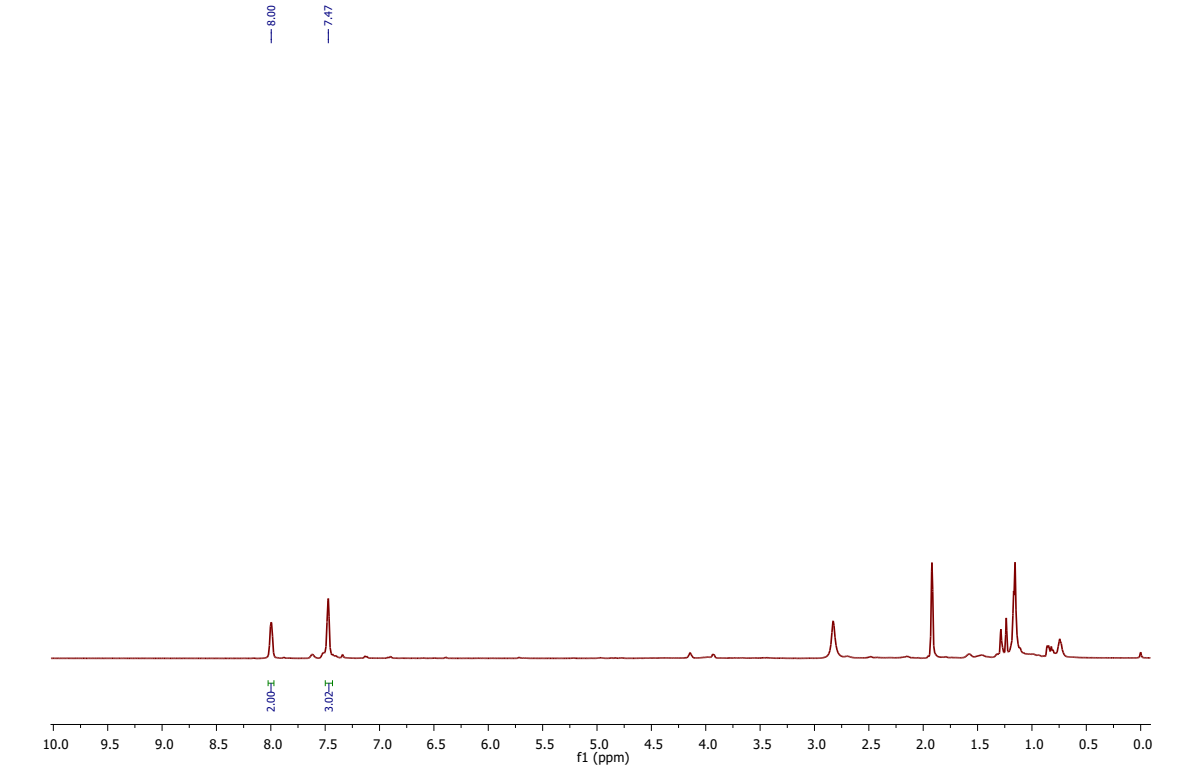

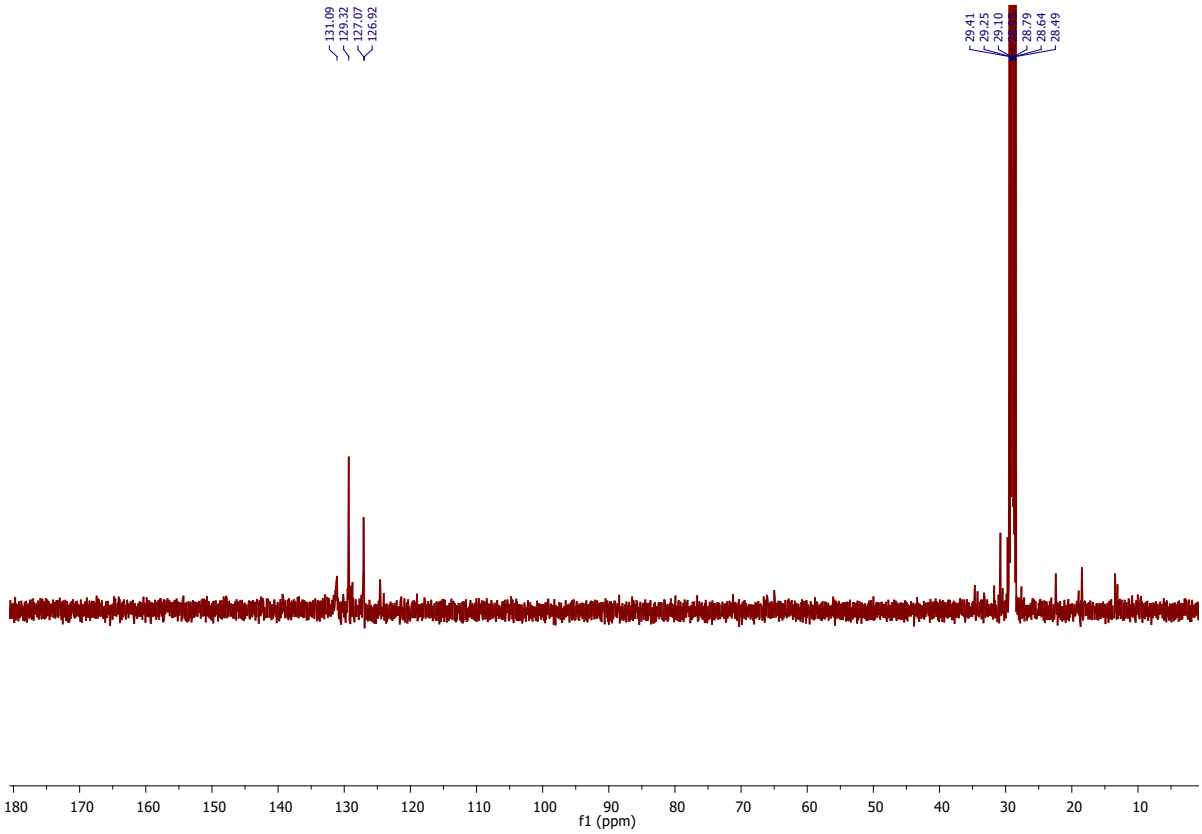

5-(4-acetyl)-1H-tetrazole (3b):

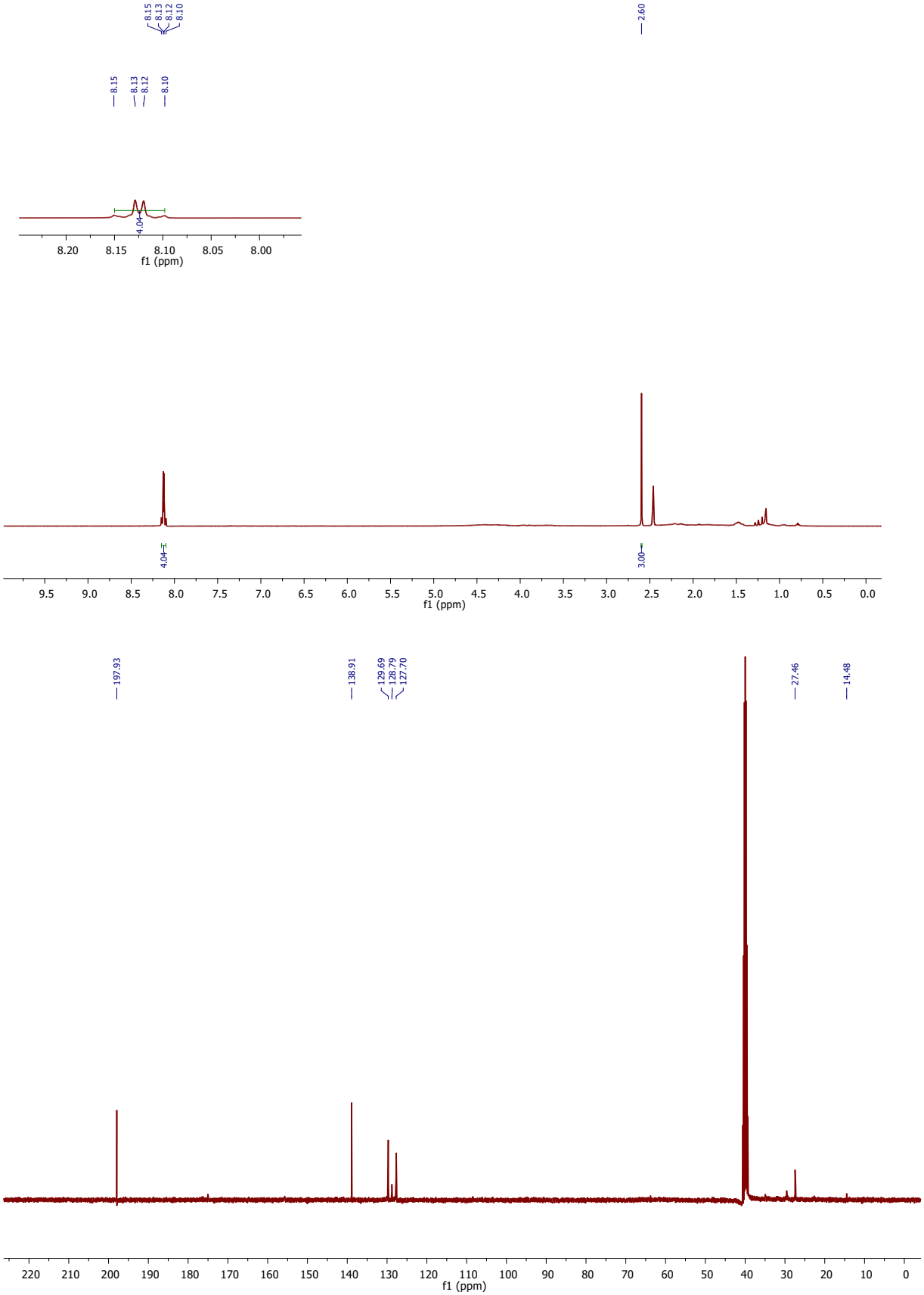

5-(4-formylphenyl)-1*H*-tetrazole (3c):

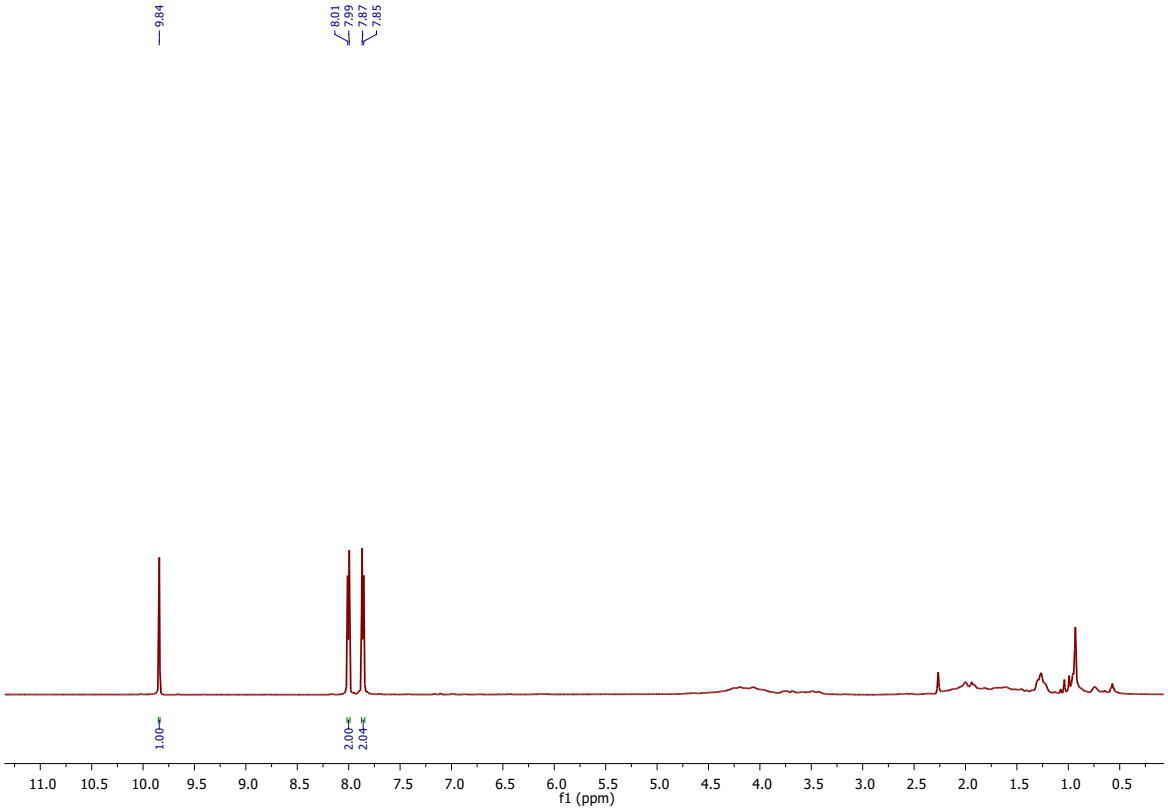

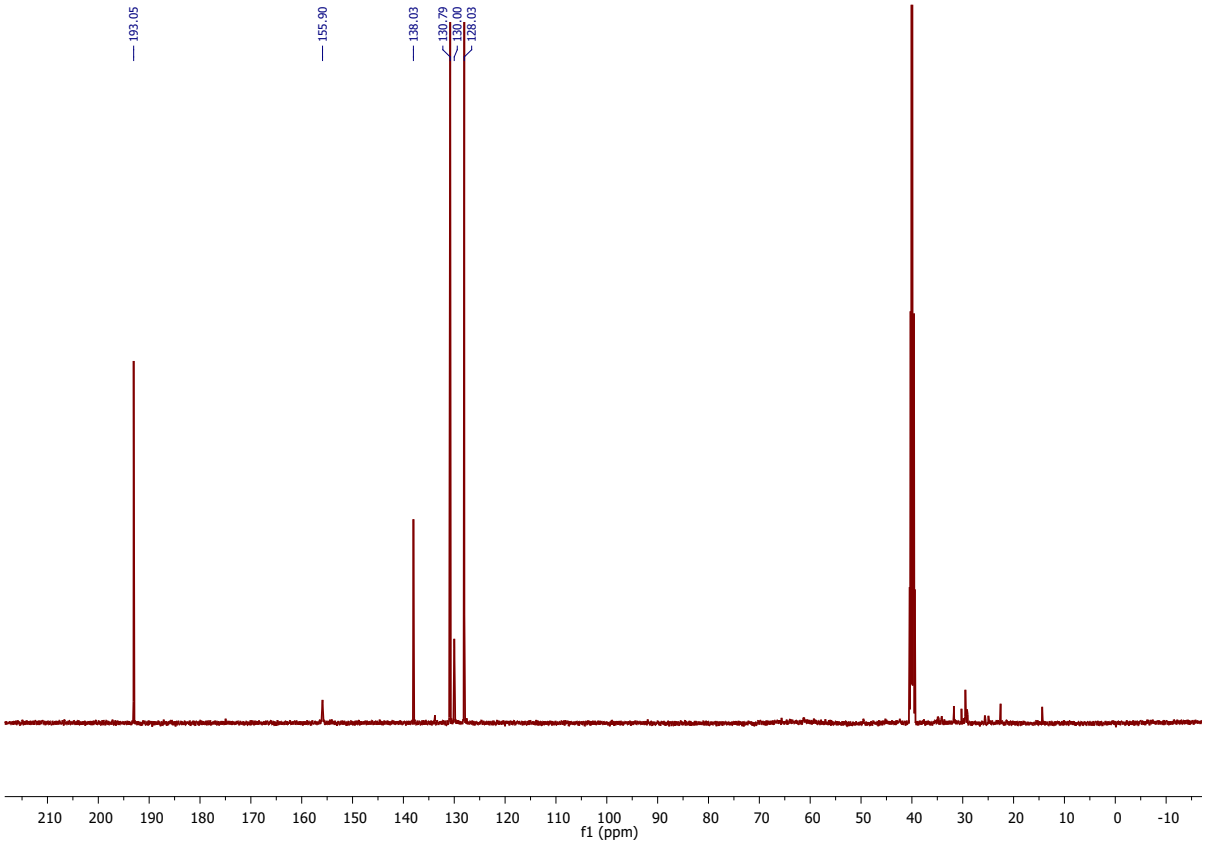

5-(4-bromophenyl)-1H-tetrazole (3d):

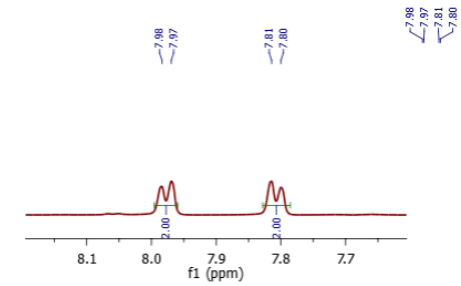

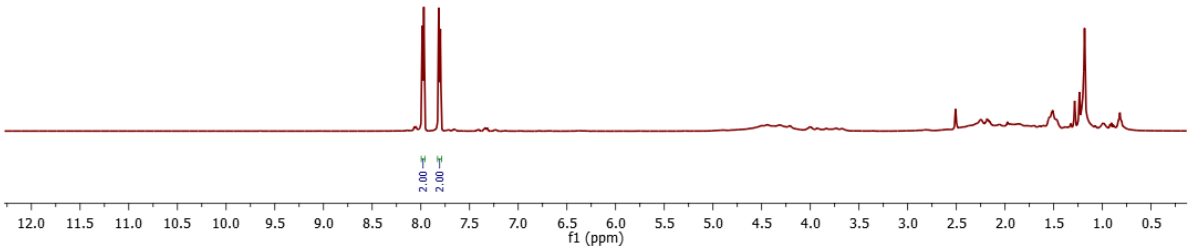

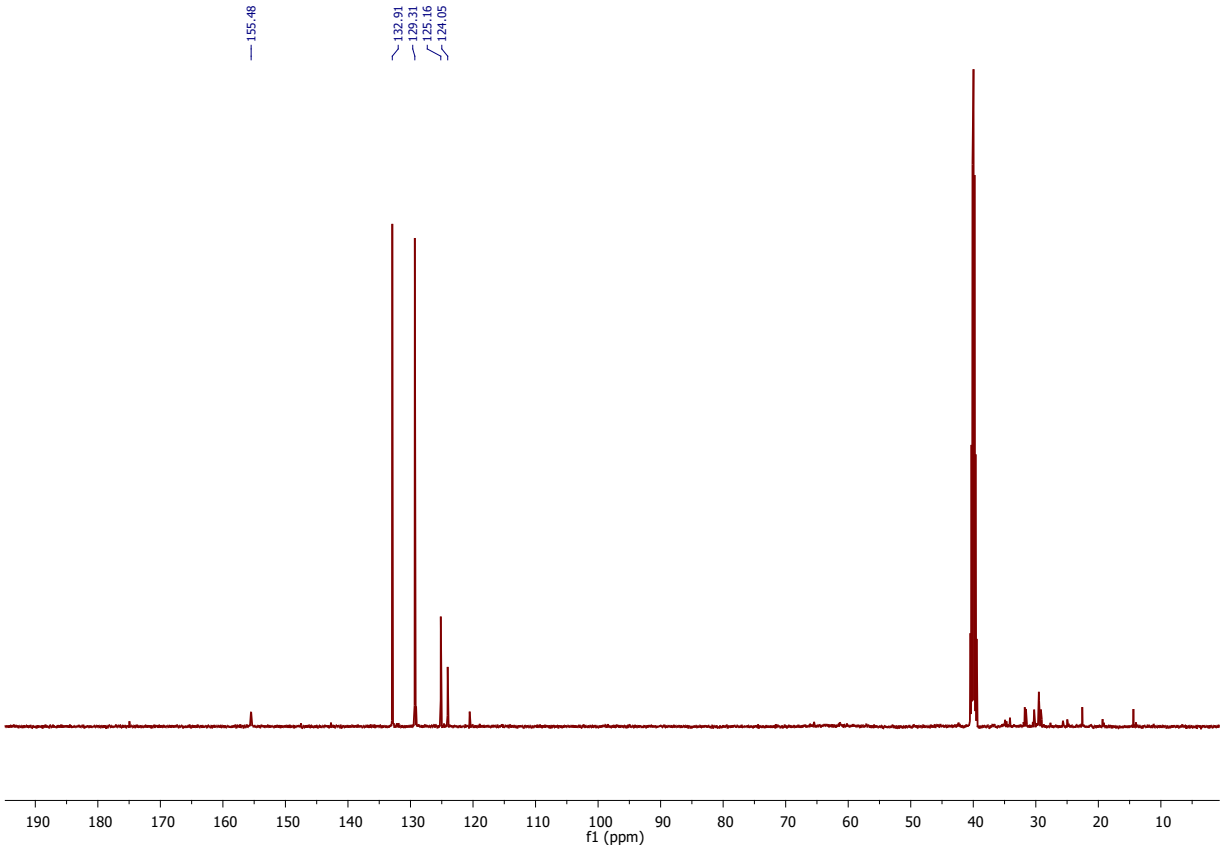

5-(2-Chlorophenyl)-1H-tetrazole (3e):

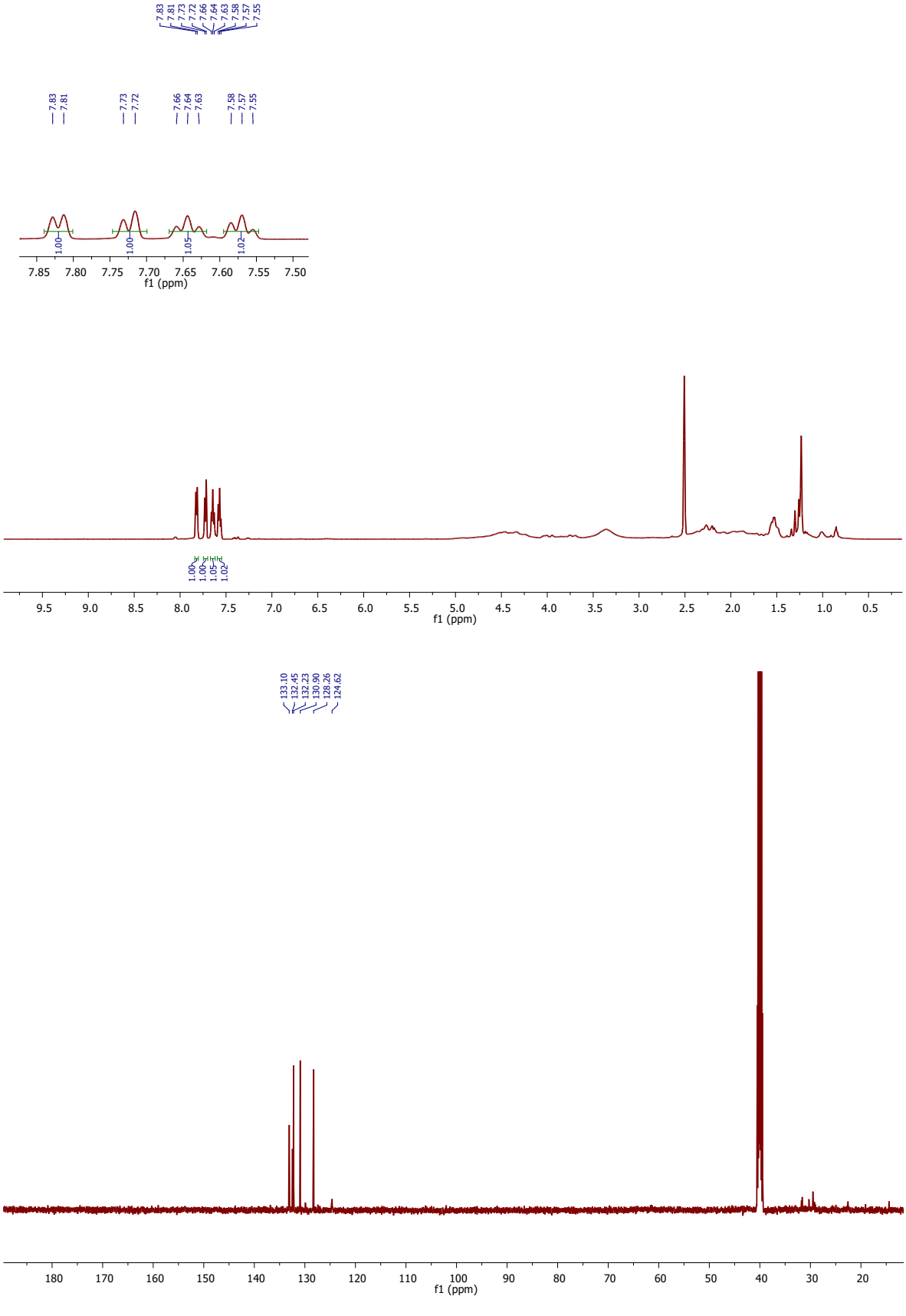

5-(4-fluorophenyl)-1H-tetrazole (3g):

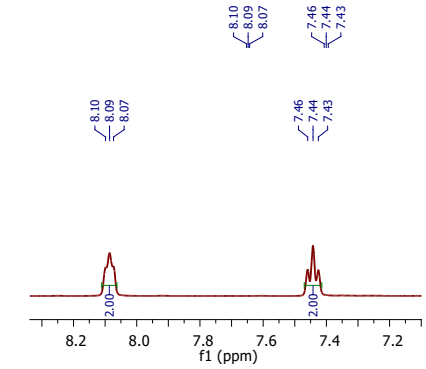

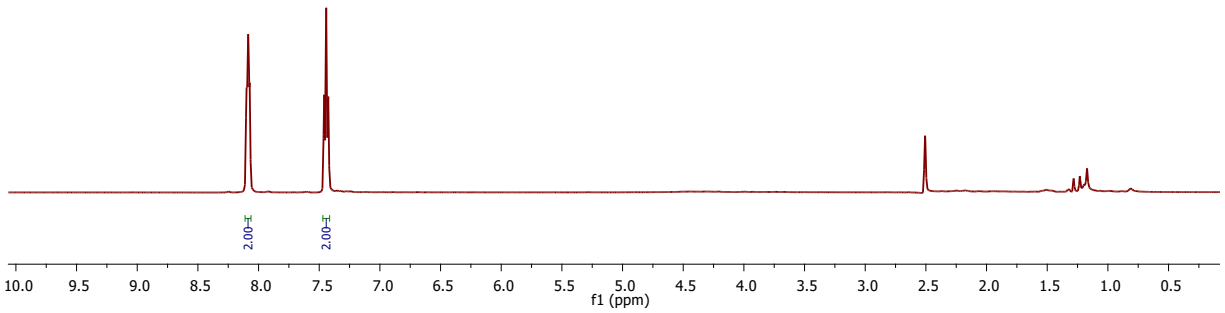

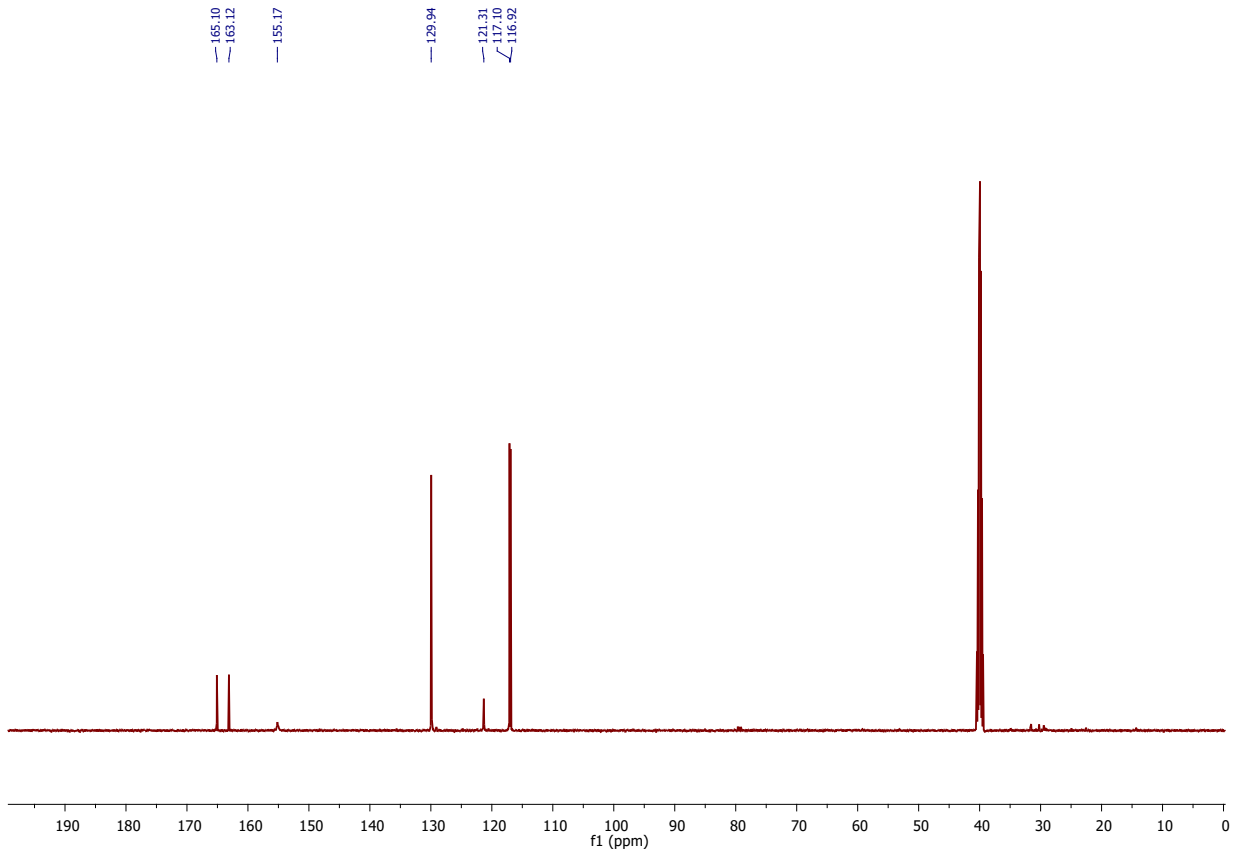

5-(3-nitrophenyl)-1*H*-tetrazole (3h):

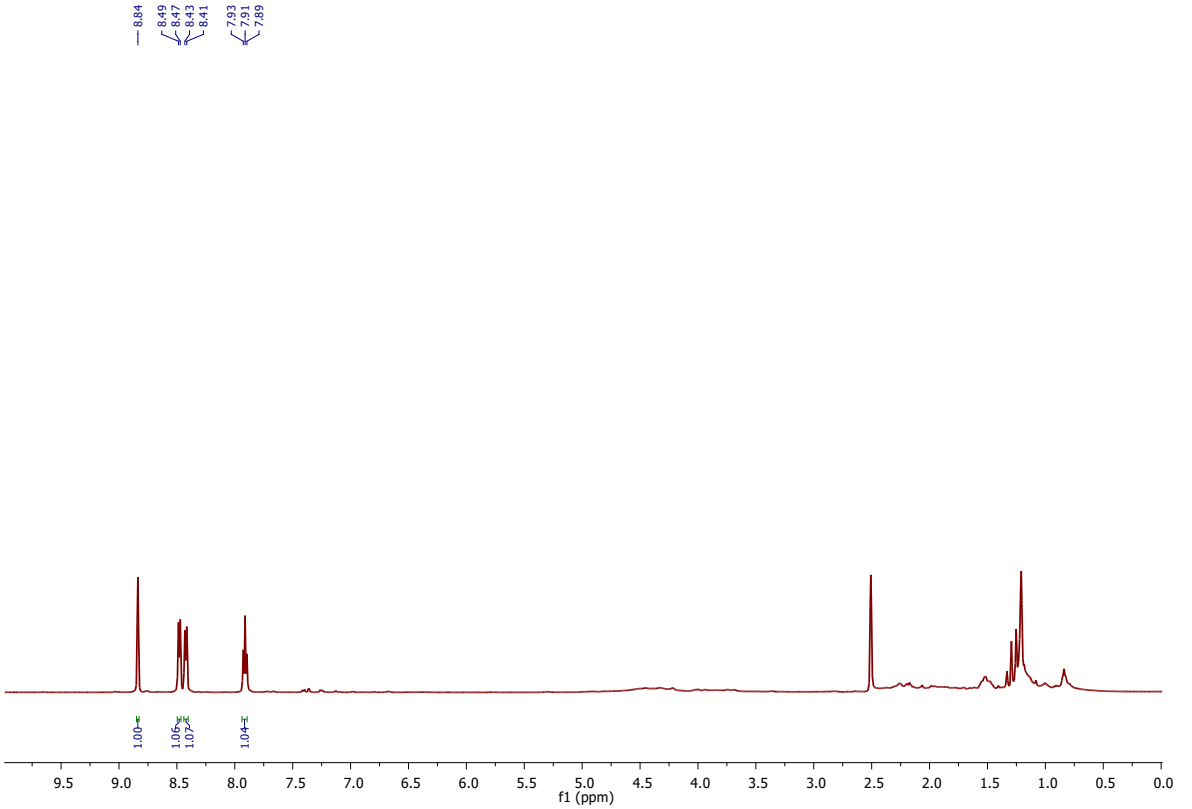

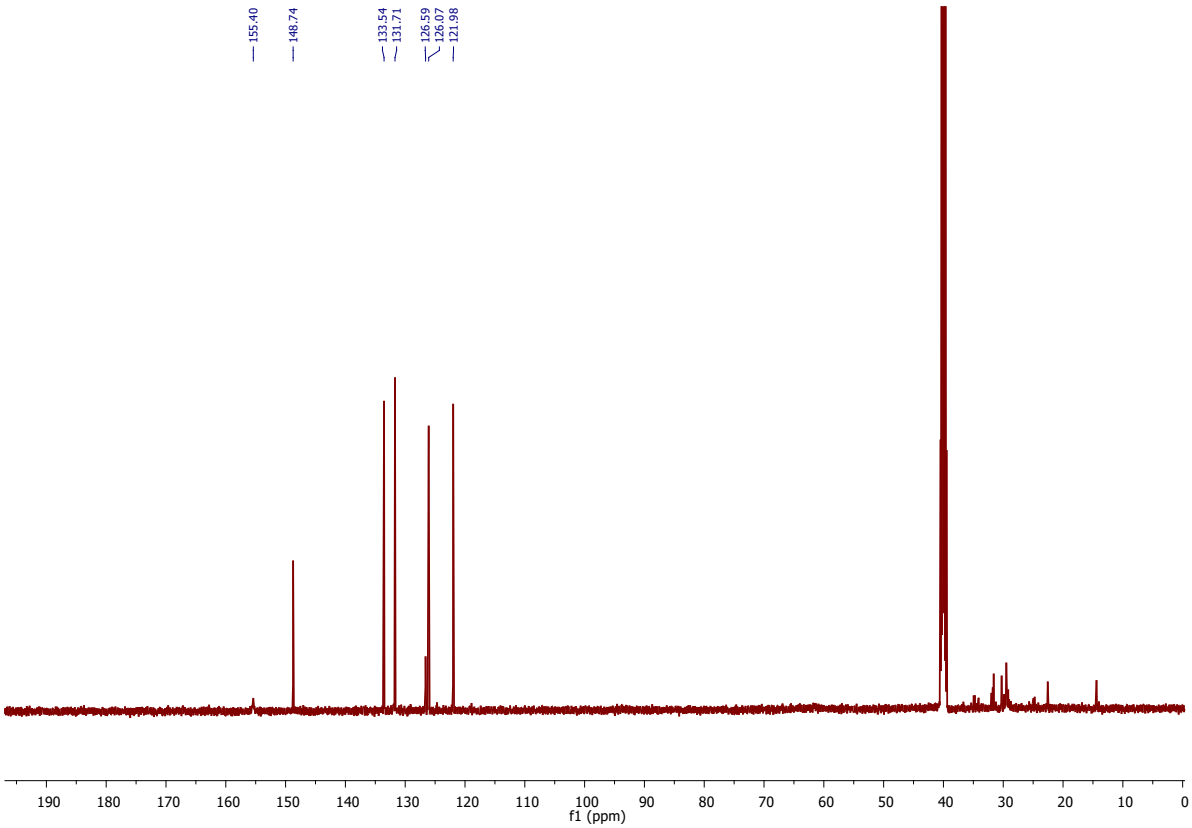

5-(4-methoxyphenyl)-1*H*-tetrazole (3i):

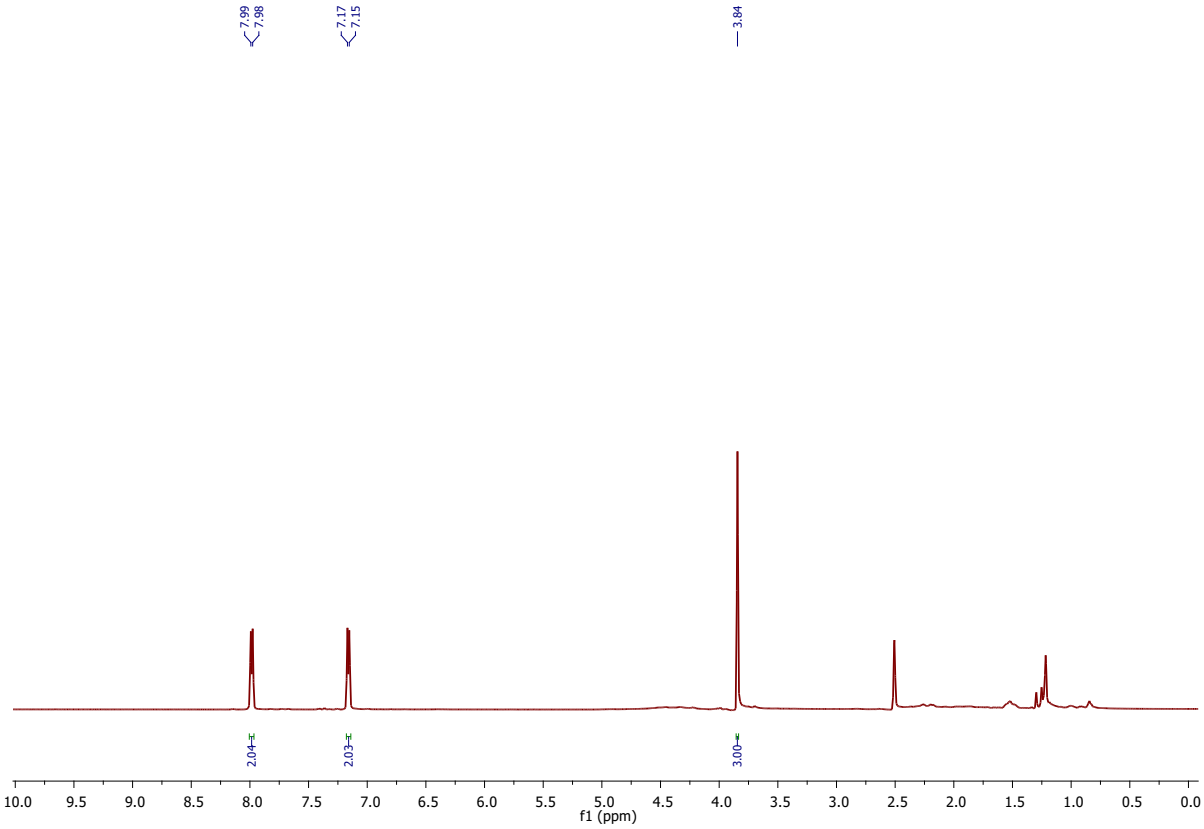

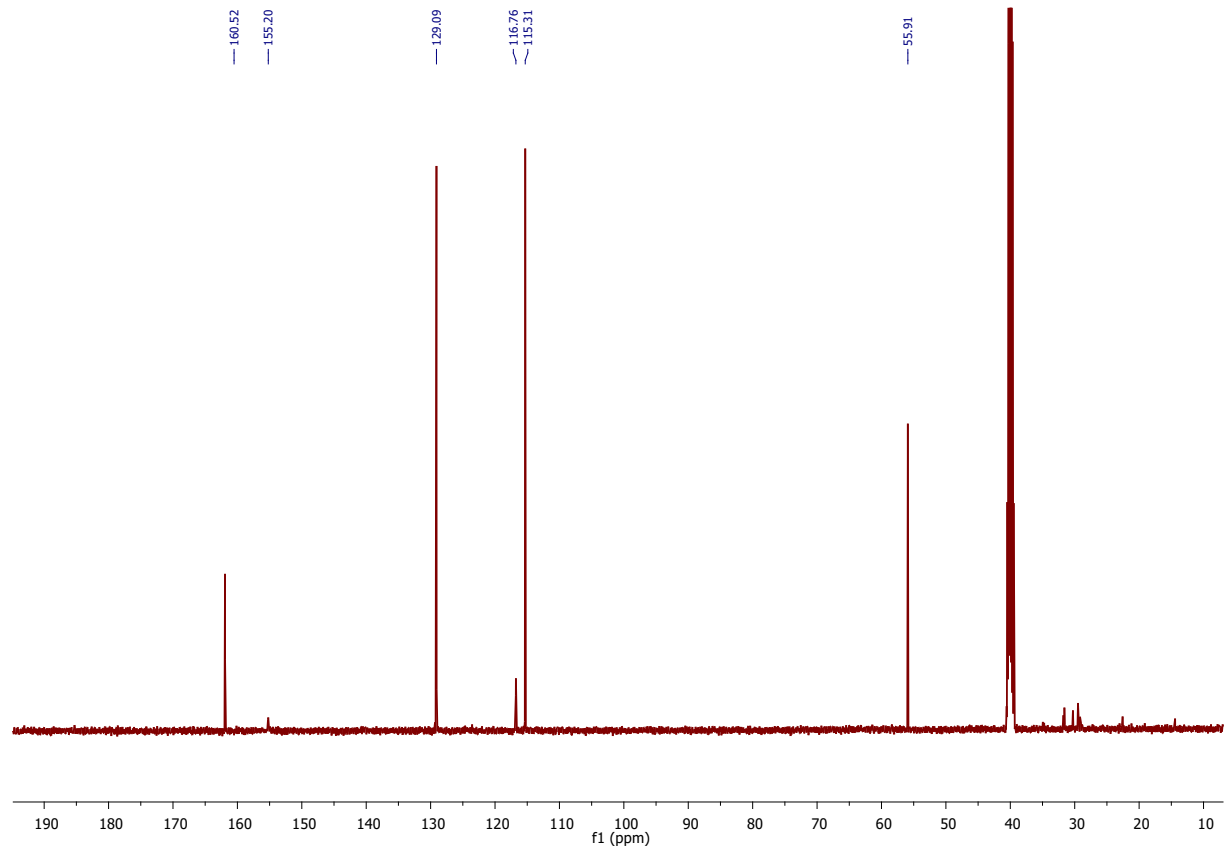

5-(4-hydroxyhenyl)-1*H*-tetrazole (3j):

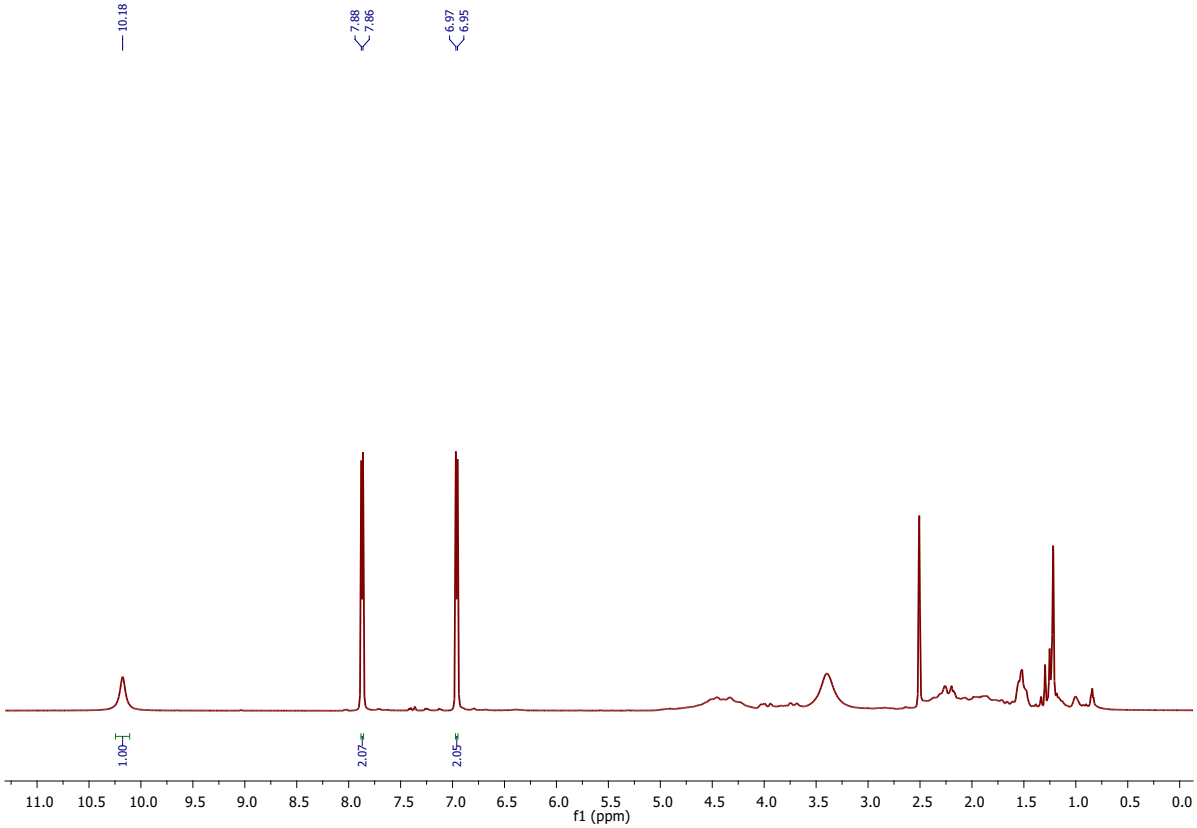

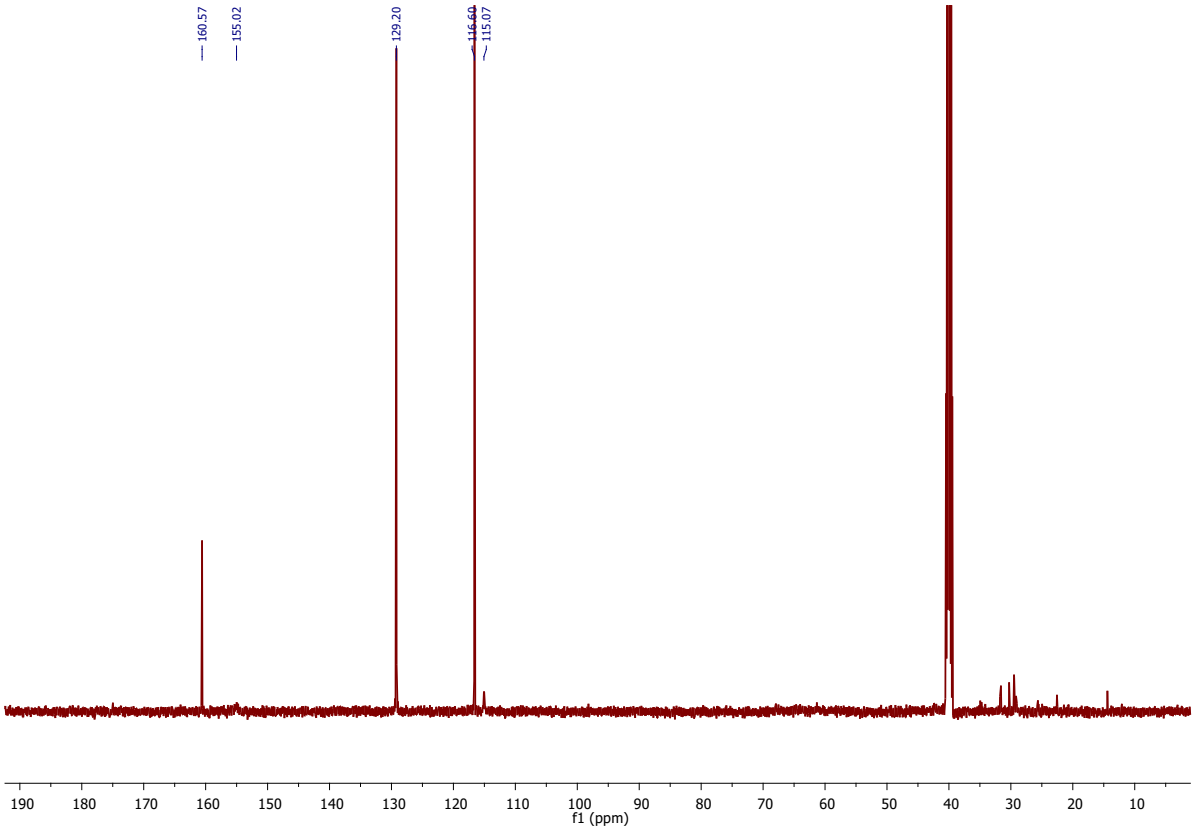

2-chloro-3-(1*H*-tetrazol-5-yl) pyridine (3l):

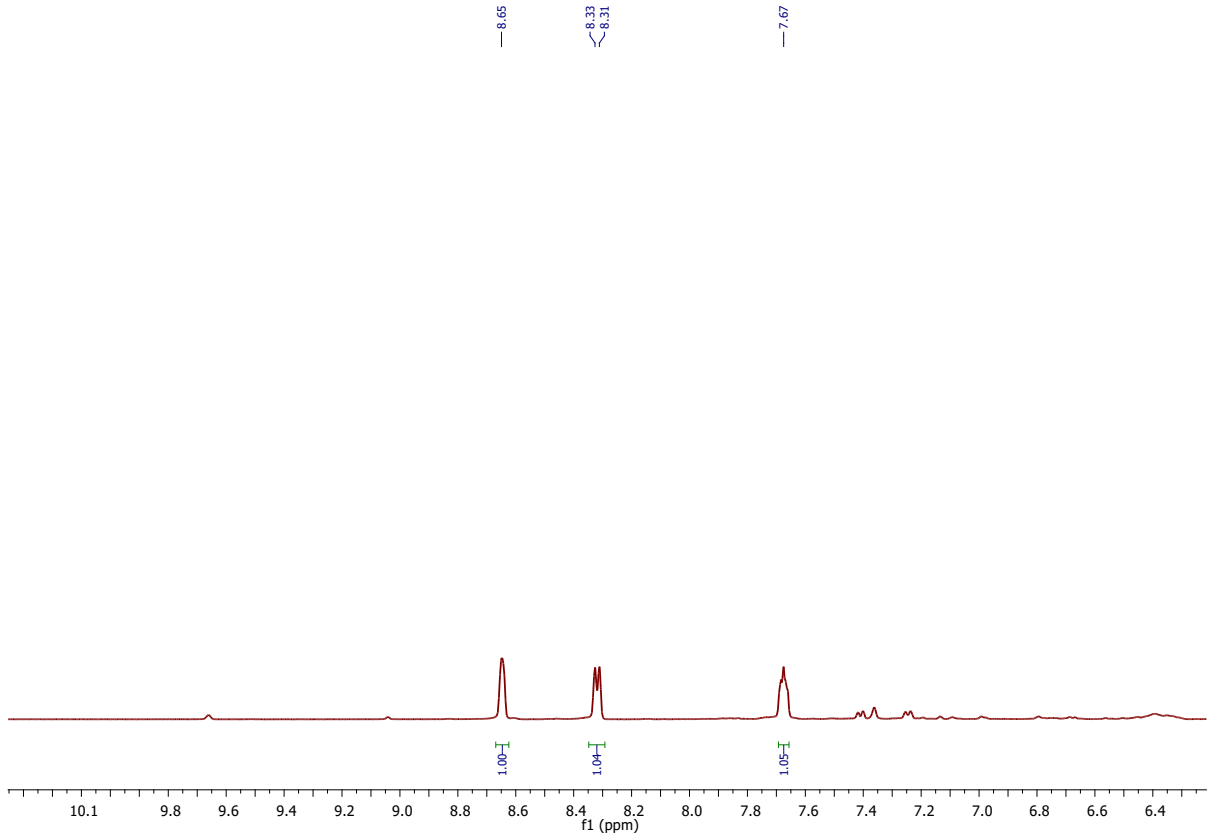

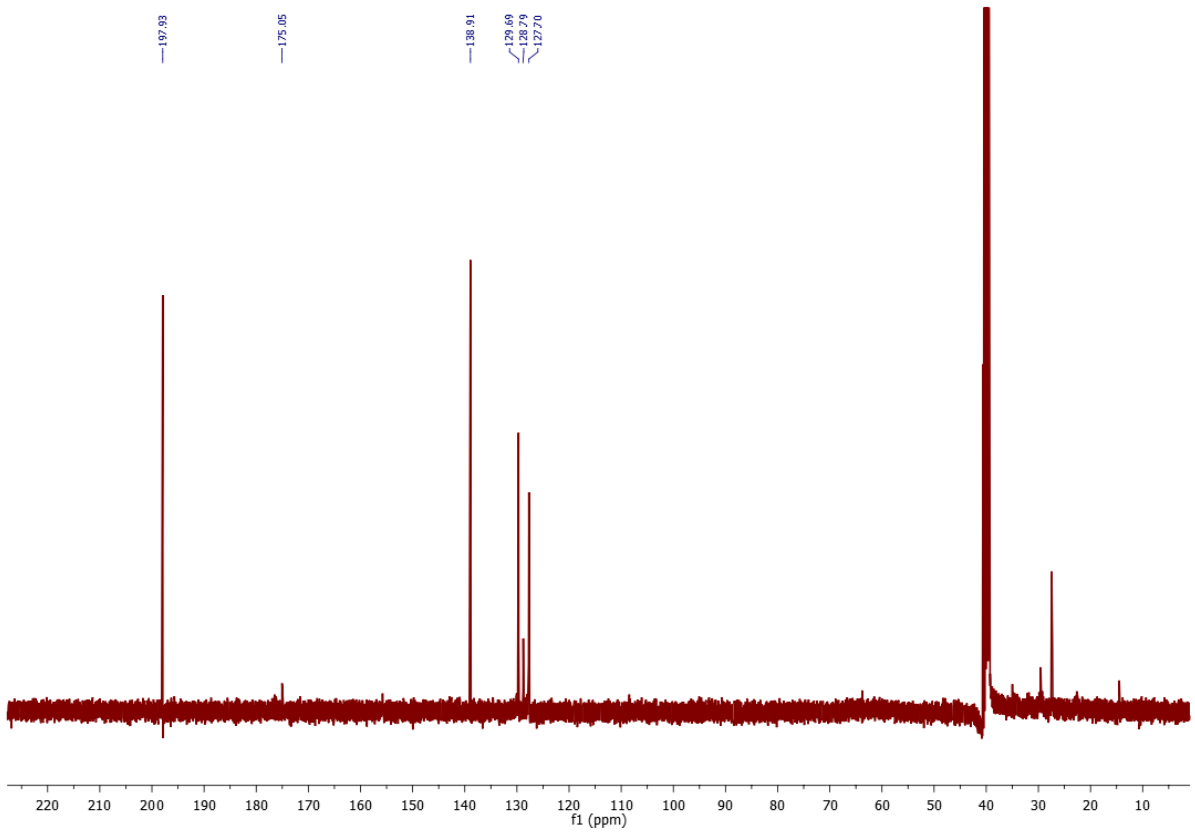

5-(thiophen-2-yl)-1*H*-tetrazole (3m):

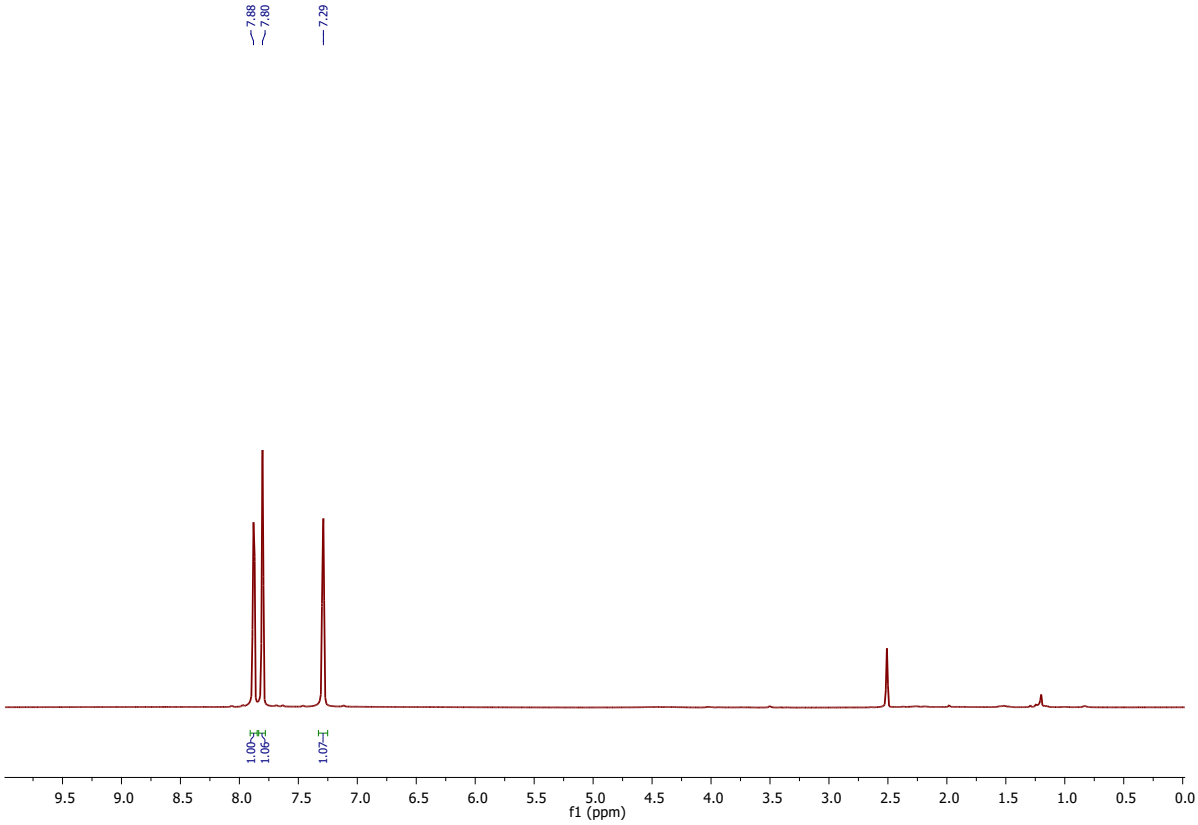

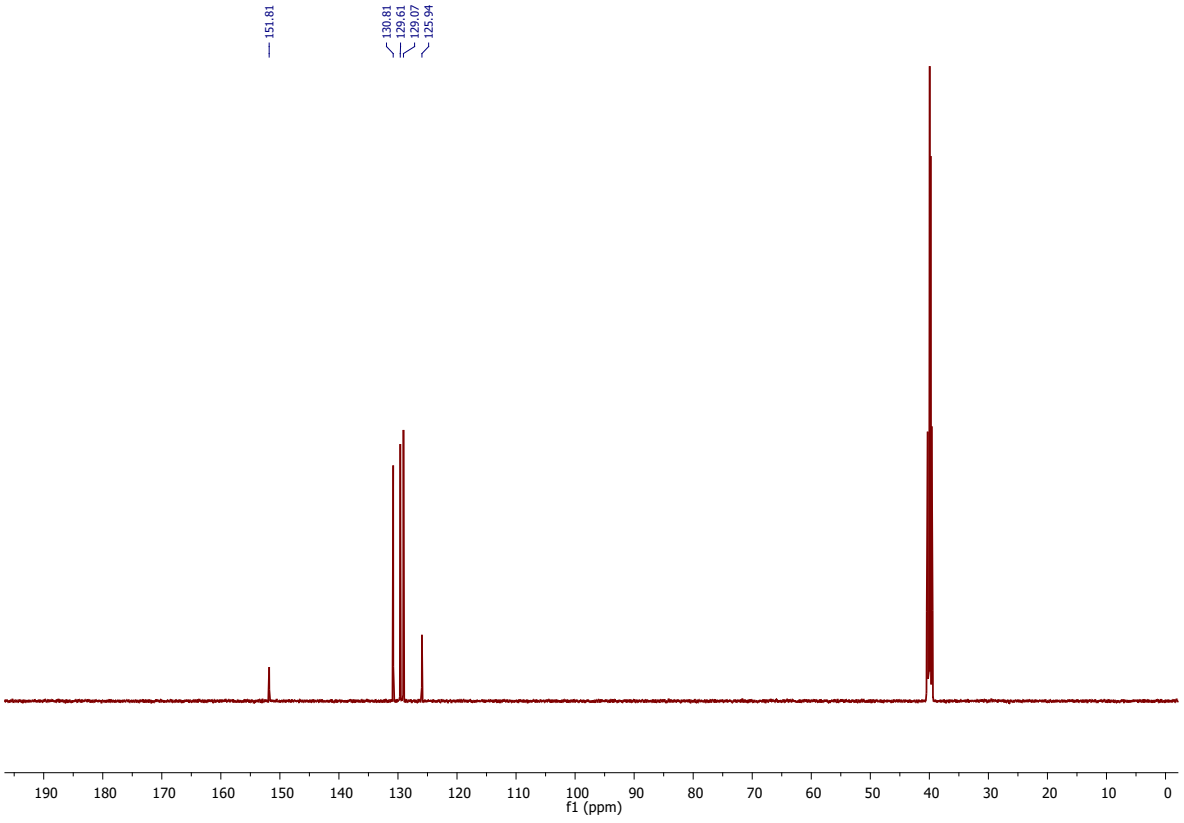

4-aminoibenzamide (5m):

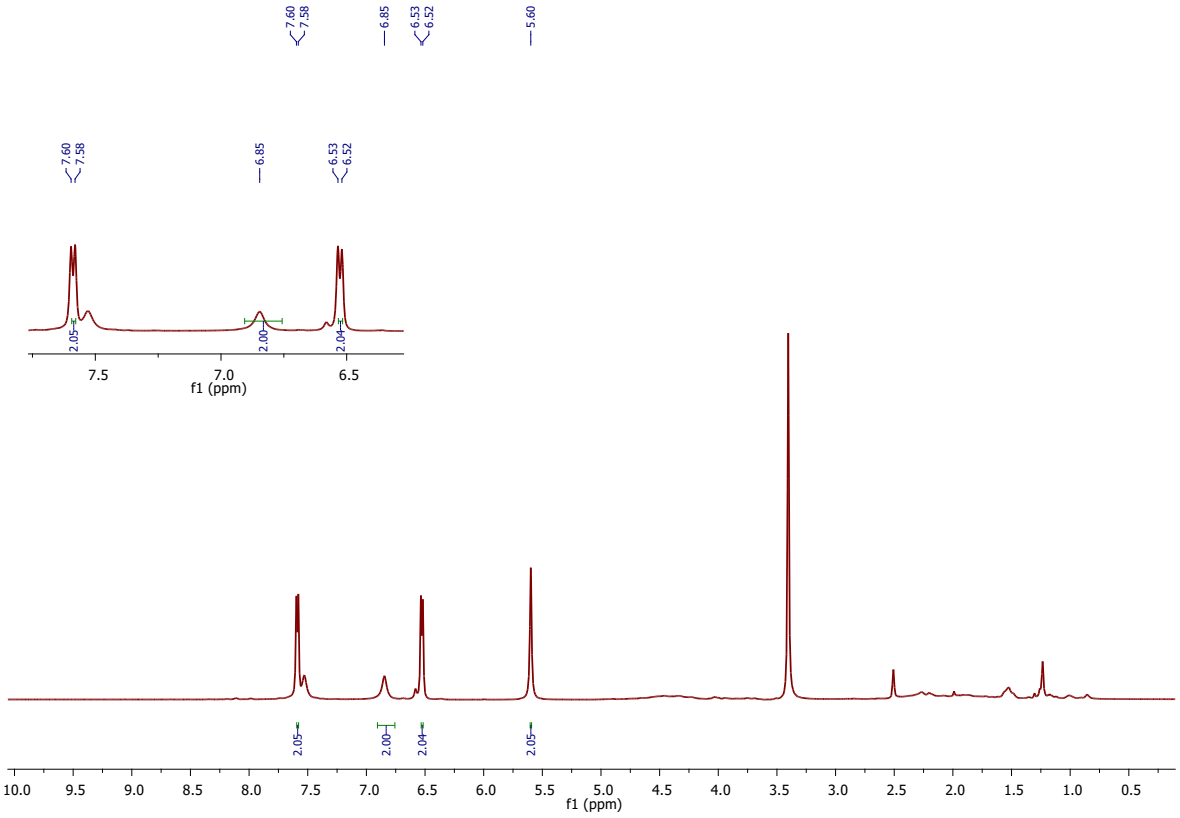

4-aminobenzohydrazide (5n):

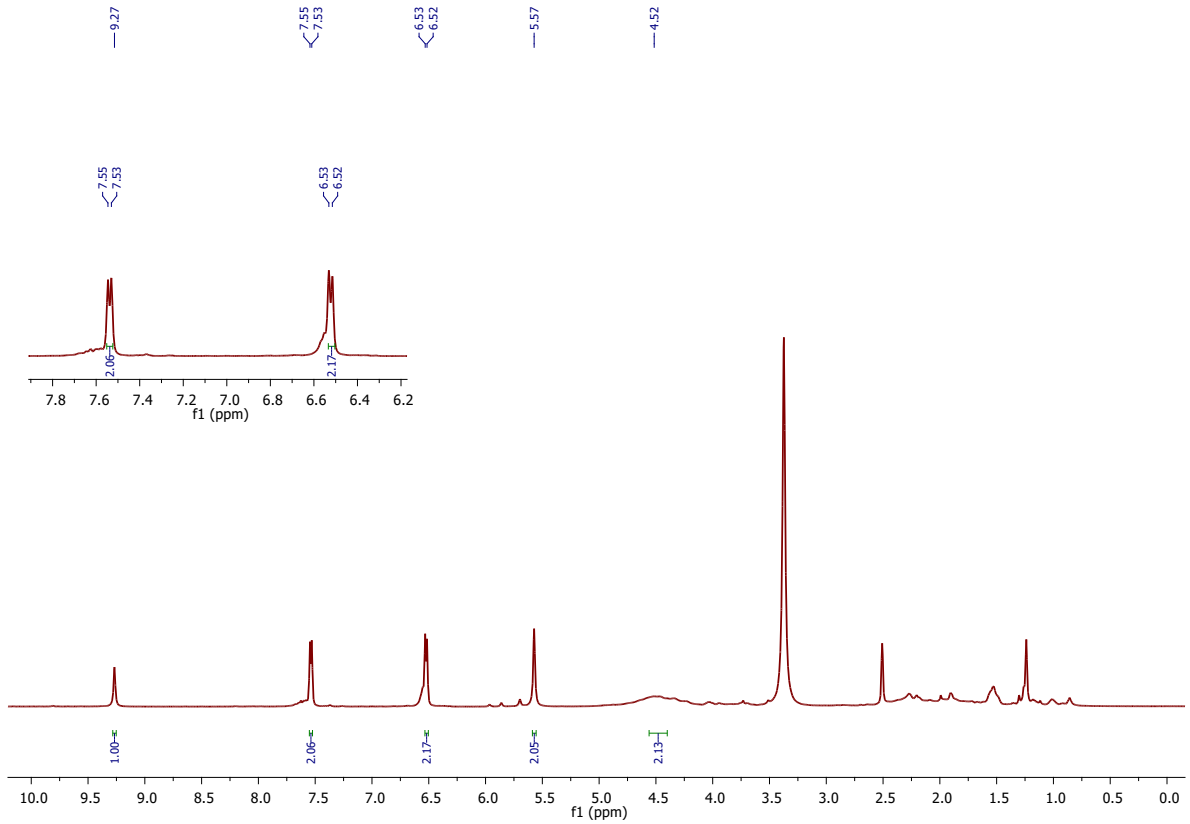

Ethyl-4-aminobenzoate [Benzocaine] (5o):